ATLAS NOTE

ATLAS-CONF-2012-094

July 9, 2012

Search for neutral MSSM Higgs bosons in $\sqrt{s} = 7$ TeV pp collisions with the ATLAS detector

The ATLAS Collaboration

Abstract

A search for the neutral Higgs bosons of the Minimal Supersymmetric Standard Model (MSSM) is reported. The analysis is based on a sample of proton-proton collisions at a centre-of-mass energy of 7 TeV recorded with the ATLAS detector at the Large Hadron Collider. The data were recorded in 2011 and correspond to an integrated luminosity of $4.7 - 4.8\,\text{fb}^{-1}$. Higgs boson decays into oppositely-charged muon or τ lepton pairs are considered for final states requiring either the presence or absence of b jets. No statistically significant excess over the expected background is observed and exclusion limits at the 95 % confidence level are derived for the production cross section of a generic Higgs boson, ϕ, as a function of the Higgs boson mass and for $h/A/H$ production in the MSSM as a function of the parameters m_A and $\tan\beta$ in the $m_{\text{h}}^{\text{max}}$ scenario with $\mu > 0$.

ATLAS-CONF-2012-094
10/07/2012

1 Introduction

Discovering the mechanism responsible for electroweak symmetry breaking is one of the major goals of the physics program at the Large Hadron Collider (LHC) [1]. In the Standard Model (SM) this mechanism requires the existence of a single scalar particle, the Higgs boson [2, 3, 4, 5, 6]. However, the mass of this particle is quadratically divergent due to quantum corrections. This problem can be solved by introducing supersymmetry, a symmetry between fermions and bosons, by which the divergent corrections to the Higgs boson mass are cancelled.

In the Minimal Supersymmetric Standard Model (MSSM) [7, 8], two Higgs doublets are necessary, coupling separately to up-type and down-type fermions. This results in five physical Higgs bosons, two of which are neutral and CP-even (h, H)[1], one of which is neutral and CP-odd (A), and two of which are charged ($H^{\pm}$). At tree level their properties can be described in terms of two parameters, typically chosen to be the mass of the CP-odd Higgs boson, m_{A}, and the ratio of the vacuum expectation values of the two Higgs doublets, $\tan\beta$. Couplings to down-type fermions are enhanced with increasing $\tan\beta$ for A and either H or h, while the corresponding couplings to up-type fermions are suppressed with increasing $\tan\beta$. Additionally, couplings to the Standard Model vector bosons are absent for A and suppressed for either H or h. This has important consequences for both production and decay of neutral MSSM Higgs bosons.

For setting of exclusion limits the analysis is evaluated in the context of the $m_{\mathrm{h}}^{\mathrm{max}}$ benchmark scenario [9] with $\mu > 0$. In the $m_{\mathrm{h}}^{\mathrm{max}}$ scenario the parameters in the $\tilde{t}$ and $\tilde{b}$ sector and the gaugino masses are fixed to obtain the maximum possible mass for the lightest CP-even Higgs boson for a given $\tan\beta$ and mass of the CP-odd Higgs boson m_A. This guarantees conservative exclusion bounds from the LEP experiments. The sign of the Higgs sector bilinear coupling μ is generally not constrained, but in the evaluation of the analysis $\mu > 0$ is chosen as this is favoured by the measurements of $(g-2)_{\mu}$.

For high $\tan\beta$ in this scenario the masses of the Higgs bosons are such that for $m_A < 125$ GeV the h and A bosons are degenerate in mass and for $m_A > 125$ GeV the H and A bosons are degenerate in mass to within a few GeV.

The most common MSSM neutral Higgs production mechanisms at a hadron collider are the b quark annihilation and gluon-fusion processes, the latter of which proceeds primarily through a b quark loop for high $\tan\beta$. Both processes have cross sections that increase with $\tan\beta$, with the b-associated production process becoming dominant at high $\tan\beta$ values. In this case the presence of a b jet in the final state can offer improved background rejection. The most common decay modes at high $\tan\beta$ are to a pair of b quarks or τ leptons, with branching ratios close to 90 % and 10 %, respectively, across the mass range considered. Additionally, the direct decay into two muons occurs rarely, with a branching ratio around 0.04 %, but it offers a clean signature.

Previous searches for neutral MSSM Higgs bosons have been performed at LEP [10], the Tevatron [11, 12, 13] and the LHC [14, 15]. In light of recent results from LHC Standard Model Higgs searches [16, 17], theoretical investigations [18] have demonstrated compatibility between a significant parameter space of the MSSM and an assumed signal at $M_h \sim 125$ GeV, consistent with the lighter CP-even MSSM Higgs boson. In this paper a search using $4.7 - 4.8\,\mathrm{fb}^{-1}$ of proton-proton collision data collected with the ATLAS detector in 2011 is presented. The $\mu^+\mu^-$ and $\tau^+\tau^-$ decay modes are considered, with the latter divided into separate search channels according to the visible particles in the decay of each τ lepton (either an electron, a muon, or one or more hadrons). Each channel is further classified according to jet multiplicity and jet flavour.

[1] By convention the lighter CP-even Higgs boson is called h, the heavier CP-even Higgs boson is called H.

2 The ATLAS detector

The ATLAS detector at the LHC is a multipurpose apparatus with a forward-backward symmetric cylindrical geometry and nearly 4π coverage in solid angle [19]. It consists of an inner detector surrounded by a thin superconducting solenoid providing a 2 T axial magnetic field, electromagnetic and hadronic calorimeters, and a muon spectrometer, incorporating three large superconducting air-core toroid magnets with bending power between 2.0 and 7.5 Tm. The inner detector covers the pseudorapidity[2] range $|\eta| < 2.5$. It consists of silicon pixel, semi-conductor micro-strip, and transition radiation tracking detectors. Lead/liquid-argon (LAr) sampling calorimeters provide electromagnetic (EM) measurements with high granularity. A hadronic (iron/scintillator-tile) calorimeter covers the central pseudorapidity range ($|\eta| < 1.7$). The end-cap and forward regions are instrumented with LAr calorimeters for both EM and hadronic energy measurements up to $|\eta| = 4.9$. A three-level trigger system is used to select events. The first-level trigger is implemented in hardware and uses a subset of the detector information to reduce the rate to at most 75 kHz. This is followed by two software-based trigger levels that together reduce the event rate to approximately 300 Hz. The trigger requirements were adjusted to changing data-taking conditions in 2011.

3 Data and Monte Carlo simulation samples

The data used in this search were recorded by the ATLAS experiment during the 2011 LHC run with proton-proton collisions at a centre-of-mass energy of 7 TeV. They correspond to an integrated luminosity of approximately 4.7 fb^{-1} ($\tau^+\tau^-$ channels) or 4.8 fb^{-1} ($\mu^+\mu^-$ channels) after data quality selection criteria to require that all relevant detector sub-systems used in this analysis were operational. The integrated luminosity has an uncertainty of 3.9 %, measured as described in References [20, 21] and based on the whole 2011 dataset.

Higgs boson production: The Higgs production mechanisms considered are gluon-fusion and b quark associated production. The cross sections for the first process have been calculated using HIGLU [22] and ggh@nnlo [23]. For b-associated production, a matching scheme described in Reference [24] is used to combine 4-flavour [25, 26] and 5-flavour [27] calculations. The masses, couplings, and branching ratios of the Higgs bosons are computed with FeynHiggs [28]. Details of the calculations and associated strong coupling constant, parton distribution function (PDF) and scale uncertainties can be found in Reference [29]. Gluon-fusion production is simulated with POWHEG [30], while b quark associated production is simulated with SHERPA [31].

The $h/A/H \to \tau^+\tau^-$ and $h/A/H \to \mu^+\mu^-$ decay modes are considered for the decay of the Higgs boson. Pseudoscalar A-boson samples for both production processes were generated, and these samples are also employed for H and h assuming the mass combinations of the m_h^{max}, $\mu > 0$ MSSM benchmark scenario and the same kinematics for the decay products. The signal samples with m_{A} closest to the computed mass of the H and h boson are used for H and h boson production for the $h/A/H \to \tau^+\tau^-$ channels, respectively.

For the $\tau^+\tau^-$ decay mode, 15 samples with Higgs boson masses in the range of 90 GeV to 500 GeV with $\tan\beta = 20$ were generated, and are scaled to the appropriate cross section for other $\tan\beta$ values.

[2] ATLAS uses a right-handed coordinate system with its origin at the nominal interaction point (IP) in the centre of the detector and the z-axis along the beam pipe. The x-axis points from the IP to the centre of the LHC ring, and the y-axis points upwards. Cylindrical coordinates (r, ϕ) are used in the transverse plane, ϕ being the azimuthal angle around the beam pipe. The pseudorapidity is defined in terms of the polar angle θ as $\eta = -\ln\tan(\theta/2)$.

The increase in the Higgs boson natural width with $\tan\beta$, of the order of 1 GeV in the range considered, is negligible compared to the experimental resolution in this channel.

For the $\mu^+\mu^-$ decay mode, seven samples with Higgs boson masses in the range of 110 GeV to 300 GeV and with $\tan\beta = 40$ were generated. Additionally, to study the $\tan\beta$ dependence of the width of the resonance, signal samples for both production modes are generated for $m_{\rm A} = 150$ GeV and 250 GeV, each at $\tan\beta = 20$ and $\tan\beta = 60$. Due to the higher resolution in this channel, signal distributions for different intermediate $m_{\rm A}$-$\tan\beta$ values are obtained using an interpolation procedure described in Section 5.

The generated Monte Carlo samples for the $h/A/H \to \tau^+\tau^-$ decay modes were passed through the full GEANT4 [32, 33] detector simulation, while the samples for the $h/A/H \to \mu^+\mu^-$ decay mode were passed through the full GEANT4 detector simulation or the ATLFast-II [32] simulation of the ATLAS detector.

Background processes: The production of W and Z/γ^* bosons in association with jets is simulated with the ALPGEN [34] and PYTHIA [35] generators, while PYTHIAB [36] is used for the production of $b\bar{b}$ samples. The $t\bar{t}$ production process is generated with MC@NLO [37]. MC@NLO and HERWIG are both used for the generation of electroweak di-boson (WW, WZ, ZZ) samples. Single-top production through the s- and t-channels, and in association with W bosons, is generated using both MC@NLO and AcerMC [38]. For all event samples described above, parton showers and hadronisation are simulated with HERWIG [39] and the activity of the underlying event with JIMMY [40]. The loop-induced $gg \to WW$ processes are generated using gg2WW [41]. Multi-jet production is generated with PYTHIA. The following PDF sets are used: CT10 [42] for MC@NLO, CTEQ6L1 [43] for ALPGEN and SHERPA and modified leading-order MRST2007 [44] for PYTHIA samples.

The τ leptons are decayed using either SHERPA or TAUOLA [45]. In all samples except the ones generated with SHERPA, initial-state and final-state radiation of photons is simulated using PHOTOS [46]. The $Z/\gamma^* \to \tau^+\tau^-$ background processes are modelled with a τ-embedded $Z/\gamma^* \to \mu^+\mu^-$ data sample described in Section 6. All generated Monte Carlo background samples were passed through the full GEANT4 simulation of the ATLAS detector.

All signal and background samples were reconstructed with the same software as used for data. To take into account the presence of multiple interactions occurring in the same and neighbouring bunch crossings (referred to as pile-up), simulated minimum bias events were added to the hard process in each generated event. Prior to the analysis, simulated events are reweighted in order to match the distribution of the average number of pile-up interactions per bunch crossing in the data.

4 Object reconstruction

An electron candidate is formed from energy deposits in the electromagnetic calorimeter associated with a track measured in the inner detector. Electrons are selected if they have a transverse energy $E_{\rm T} > 15$ GeV, lie within $|\eta| < 2.47$, but outside of the transition region between the barrel and end-cap calorimeters ($1.37 < |\eta| < 1.52$), and meet quality requirements based on the expected shower shape [47].

A muon candidate is formed from a high-quality track measured in the inner detector matched to hits in the muon spectrometer [48]. Muons are required to have a transverse momentum of $p_{\rm T} > 10$ GeV and to lie within $|\eta| < 2.5$. In addition, the point of closest approach of the inner detector track must be no further than 1 cm from the primary vertex[3], as measured along the z-axis. This

[3]The primary vertex is defined as the vertex with the largest Σp_T^2 of the associated tracks.

requirement reduces the contamination due to cosmic-ray muons and beam-induced backgrounds.

Identified electrons and muons are required to be isolated from additional activity in the inner detector and the calorimeter. The scalar sum of the transverse momenta of all tracks from the same vertex as the lepton, with p_{T} above 1 GeV and located within a cone of radius[4] $\Delta R = 0.4$ around the lepton direction, must be less than 6 % of the lepton energy for the $\tau^+\tau^-$ channels, or less than 10 % for the $\mu^+\mu^-$ channels. The sum excludes the track associated to the lepton itself. In addition, a pile-up-dependent requirement on the calorimetric energy within a cone of radius $\Delta R = 0.2$ around the lepton direction, excluding the energy associated to the lepton itself, is applied in the $\tau^+\tau^-$ channels.

Jets are reconstructed using the anti-k_{t} algorithm [49] with a radius parameter of $R = 0.4$, taking three-dimensional noise-suppressed clusters in the calorimeters [50] as input. The jet energy is calibrated using corrections derived from Monte Carlo applied to these constituent clusters [51, 52]. This calibration is validated by test beam and collision data. Reconstructed jets with $E_{\mathrm{T}} > 20$ GeV and within $|\eta| < 2.5$ are selected. Events are discarded if a jet is associated with out-of-time activity or calorimeter noise. To reduce the effect of pile-up, at least three-quarters of a jet's transverse momentum, as measured by the sum of the transverse momenta of the associated tracks, must come from tracks matched to the primary vertex [53]. Jets are tagged as originating from a b quark based on the impact parameter of associated tracks and the reconstruction of b-hadron decays inside the jet. A multivariate algorithm, which is based on a neural network, is used in this analysis [54].

Hadronic decays of τ leptons, which are labelled τ_{had}, are characterised by the presence of one, three or in rare cases more charged pions accompanied by a neutrino and possibly neutral pions, resulting in a collimated shower profile in the calorimeters and only a few nearby tracks. The visible decay products are then combined into τ jet candidates. Candidates are reconstructed as jets, which are re-calibrated to account for the different calorimeter response to hadronic τ decays compared to hadronic jets. Information on the collimation, isolation, and shower profile is combined into a boosted decision tree discriminant to reject backgrounds from jets [55]. In this analysis, three selections with identification efficiency of about 60 %, 45 % and 35 % are used. The rejection factor against jets varies from about 20 for the highest identification efficiency selection to about 300 for the lowest. A τ jet candidate must lie within $|\eta| < 2.5$, have a transverse momentum greater than 20 GeV, one or three associated tracks (with $p_T > 1$ GeV), and a total charge of ± 1. Dedicated electron and muon veto algorithms are used.

Leptonic decays of τ leptons, which are labelled τ_{lep} , are characterised by the presence of one electron or muon and two neutrinos. Leptonic τ decays including an electron or muon are labelled τ_{e} or τ_{μ} respectively.

When different objects selected according to the above criteria overlap with each other geometrically (within $\Delta R < 0.2$), only one of them is considered for further analysis. The overlap is resolved by selecting muon candidates, electron candidates, τ jet candidates and jet candidates in this order of priority.

The magnitude and direction of the missing transverse momentum [56], $E_{\mathrm{T}}^{\mathrm{miss}}$, is reconstructed including contributions from muon tracks and energy deposits in the calorimeters. Clusters of calorimeter cells belonging to jets (including τ jets) with $p_{\mathrm{T}} > 20$ GeV are calibrated to the hadronic energy scale. Calorimeter cells not associated with any object are also considered and are calibrated at the electromagnetic energy scale. The contributions of muons to $E_{\mathrm{T}}^{\mathrm{miss}}$ are calculated differently for isolated and non-isolated muons, to properly account for the energy deposited by muons in the calorimeters.

[4] $\Delta R = \sqrt{(\Delta\eta)^2 + (\Delta\phi)^2}$, where $\Delta\eta$ is the difference in pseudorapidity of the two objects in question, and $\Delta\phi$ is the difference between their azimuthal angles.

5 The $\mu^+\mu^-$ decay channel

The search for MSSM Higgs bosons in the $\mu^+\mu^-$ decay channel is complicated by the small branching fraction of the $h/A/H \to \mu^+\mu^-$ decay and considerable background rates. The low signal-to-background ratio is compensated to some extent by the very clean signature of the $\mu^+\mu^-$ final state in the detector. Furthermore, searches in this channel profit from the good mass resolution.

Signal and background processes: The signature of the $h/A/H \to \mu^+\mu^-$ decay is characterised by a pair of isolated muons with high transverse momenta and opposite charge. In the b quark associated production mode, the final state can be further characterised by the presence of one or two low-p_{T} b jets. The missing transverse momentum is small and of the order of the resolution of the $E_{\mathrm{T}}^{\mathrm{miss}}$ measurement.

Several background processes are considered in this analysis. The dominant background is $Z/\gamma^* \to \mu^+\mu^-$ from either the Drell-Yan continuum or produced in association with jets. In particular, Z/γ^* production in association with b quarks is an irreducible background for the b quark associated Higgs production. The $Z/\gamma^* \to \tau^+\tau^-$ decay with a subsequent decay of τ leptons to two muons is also taken into account.

In addition to the Z/γ^* background, the production of $t\bar{t}$, $b\bar{b}$, W+jets, WW and single top quark events is considered. When b jets are required in the $\mu^+\mu^-$ final state, $t\bar{t}$ production becomes the second most important background after $Z/\gamma^* \to \mu^+\mu^-$.

Event selection: Events considered in the $\mu^+\mu^-$ analysis must pass a single muon trigger with a transverse momentum threshold of 18 GeV. At least one reconstructed muon is required to be matched to the η–ϕ region of the trigger, and this muon is required to have $p_{\mathrm{T}} > 20$ GeV to be in the plateau region of the trigger efficiency. In each event at least one other muon of opposite charge is required to be reconstructed with $p_{\mathrm{T}} > 15$ GeV.

A muon pair is formed using the two highest-p_T muons of opposite charge. This muon pair is required to have an invariant mass greater than 70 GeV. No explicit rejection of events containing more than two muons is applied in order to retain $\mu^+\mu^-$ events accompanied by b jets. Events having a missing transverse momentum greater than 40 GeV are rejected.

The large background provided by Z/γ^* boson decays can be efficiently reduced by requiring that the event contains at least one jet which is tagged as a b jet. However, due to the low transverse momentum of b jets in signal events, this requirement also results in a significant loss of the signal. To avoid such a loss in sensitivity, the analysis is divided into a channel with no identified b jets and a channel with at least one identified b jet based on a working point of the b-tagging algorithm which has a signal efficiency of 70 % in simulated $t\bar{t}$ events.

Figure 1 shows the $\mu^+\mu^-$ invariant mass distribution from both data and simulated background processes for selected events with and without b jets. The b-vetoed selection is characterised by high statistics due to the dominant contribution from Z/γ^* decays which leads to a rather low signal-to-background ratio. Remaining backgrounds include WW and $t\bar{t}$ production whose contributions are roughly two orders of magnitude lower. The two dominant background processes in the b-tagged selection are Z/γ^* and $t\bar{t}$ production. The b-tagged selection offers a better signal-to-background ratio but suffers from low statistics.

Background modelling: The final observable in the $\mu^+\mu^-$ decay channel is the invariant mass distribution. A hypothetical signal would be present as a small resonance on top of the high-mass tail of the

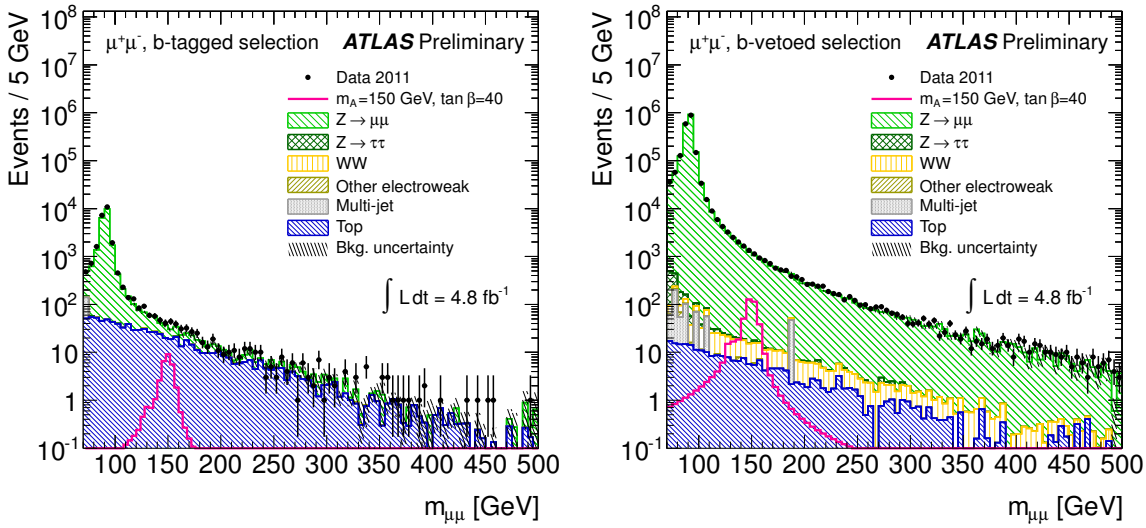

Figure 1: Final mass distributions for the $h/A/H \to \mu^+\mu^-$ final state. The invariant mass distribution of the two muons is shown for the b-tagged (left-hand side) and the b-vetoed selection (right-hand side). The data are compared to the background expectation and an added hypothetical MSSM signal ($m_{\mathrm{A}} = 150$ GeV, $\tan\beta = 40$). Simulated backgrounds are shown for illustration purposes. The background uncertainties include the statistical uncertainties only.

Z boson superimposed on a continuous contribution from non-resonant backgrounds such as $t\bar{t}$. The Z/γ^* process dominates the background with a relative fraction of 99.9 % for the b-vetoed selection and 95.8 % for the b-tagged selection. In the b-vetoed selection the non-resonant background is composed of $t\bar{t}$, W^+W^- and $b\bar{b}$ events and contributes 0.1 %; in the b-tagged selection the non-resonant background is dominated by $t\bar{t}$ events and contributes 4.2 %.

The background in this final state is estimated in a data-driven way. By scanning over the $\mu^+\mu^-$ invariant mass distribution, local sideband fits provide the expected background estimate in the mass region of interest. To this end, a parameterisation of the background shape is fit to the $\mu^+\mu^-$ invariant mass distribution in ranges determined to be sufficiently large. A search window to either side of the mass point being investigated is excluded from the fit. The widths of the search windows are motivated by the expected signal width for each point in the scanned m_{A}–$\tan\beta$ grid and account for asymmetries in the signal invariant mass distribution. The upper and lower boundaries of the search windows are defined by the $m_{\mu\mu}$ values where the signal model predictions are 10 % of their maximum.

The parameterisation of the $\mu^+\mu^-$ invariant mass distribution, $f_B(x)$, is given by

$$f_B(x, N, A, B, M_Z, \Gamma_Z, \sigma) = N \cdot \left[f_Z(x, A, B, M_Z, \Gamma_Z) \otimes f_{Gauss}(x, \sigma) \right], \tag{1}$$

where x represents the running invariant mass and $\otimes$ the convolution operator. The function f_Z describing the Z/γ^* production is

$$f_Z(x, A, B, M_Z, \Gamma_Z) = A\frac{1}{x^2} + B\frac{x^2 - M_Z^2}{\left(x^2 - M_Z^2\right)^2 + M_Z^2\Gamma_Z^2} + \frac{x^2}{\left(x^2 - M_Z^2\right)^2 + M_Z^2\Gamma_Z^2}. \tag{2}$$

This is convolved with a Gaussian distribution accounting for the finite mass resolution. The function f_Z is a simplification of the pure γ^* and Z propagators, including Z-γ^* interference contributing to

the process $q\bar{q} \to Z/\gamma^* \to \mu^+\mu^-$, and hence in principle only describes the background from Z/γ^* production. The parameterisation f_B is found to be a good approximation of the shape of the total $\mu^+\mu^-$ background even in the b-tagged selection, which has non-negligible contributions from physics processes other than Z/γ^*.

In total, the fit function f_B has six free parameters. The total normalization of the curve is described by the parameter N, parameters A and B represent the relative normalisations of the γ^* and Z-γ^* contributions with respect to the Z term. M_Z represents the Z mass, and the natural width of the Z resonance, Γ_Z, is fixed to $\Gamma_Z = 2.4952$ GeV [57]. The parameter σ represents the mean $\mu^+\mu^-$ mass resolution in the muon reconstruction.

For every point on the m_{A}–$\tan\beta$ grid, a binned likelihood fit of f_B to the data is performed and a point-by-point estimation of the fit parameters results in the total background estimate. The uncertainty on the background estimate is obtained from the confidence contour of the fit, given by a variation of the χ^2 by one standard deviation.

The background model is validated from goodness-of-fit studies using the χ^2 normalised to the number of degrees of freedom (χ^2/DoF) and the χ^2 probability ($P(\chi^2)$). In addition, the background model is extended by Bernstein polynomials of different orders to test if additional degrees of freedom change either χ^2/DoF or $P(\chi^2)$, which would hint at problems in the shape modelling. Further validation of the capability of the model to describe the shape of the data is performed by varying the fit ranges for certain mass points and accounting for the fit residuals. The goodness-of-fit studies do not show a significant mismodeling of the background beyond the statistical fluctuations for either the b-vetoed or the b-tagged selection.

Figure 2 compares the data with the background estimate predicted from sideband fits in both the b-vetoed and b-tagged selections for the signal mass point $m_{\mathrm{A}} = 150$ GeV and $\tan\beta = 40$. The data fluctuate around the background prediction leading to local bin-by-bin significances of typically less than $2\,\sigma$. Table 1 shows the number of observed events in the fit range around the mass point $m_{\mathrm{A}} = 150$ GeV compared to the number of background events predicted by the sideband fits in the b-vetoed and b-tag selections, respectively. In addition, the number of expected signal events produced in gluon-fusion or in association with b quarks is shown for $\tan\beta = 40$. The numbers shown are for illustration purposes only; the full shape information of the invariant mass distribution is used to obtain the final result.

	b-tagged selection	b-vetoed selection
Mass Point	$m_A = 150$ GeV	
Fit Range	[110, 200] GeV	
Background	980 ± 48	35890 ± 563
$b\bar{b}h/A/H \to \mu\mu$	28.3 ± 3.2	271 ± 31
$gg \to h/A/H \to \mu\mu$	2.34 ± 0.37	141 ± 15
Data	985	36044

Table 1: The number of events observed in data and the expected number of signal and background events in the $h/A/H \to \mu^+\mu^-$ channel. The number of background events is predicted from sideband fits to the $\mu^+\mu^-$ invariant mass distribution in the fit range around the signal mass point $m_{\mathrm{A}} = 150$ GeV for both the $h/A/H \to \mu^+\mu^-$ b-vetoed and b-tagged channels. The number of expected signal events produced in gluon-fusion or in association with b quarks is shown for $\tan\beta = 40$. The uncertainty is derived from the fit results.

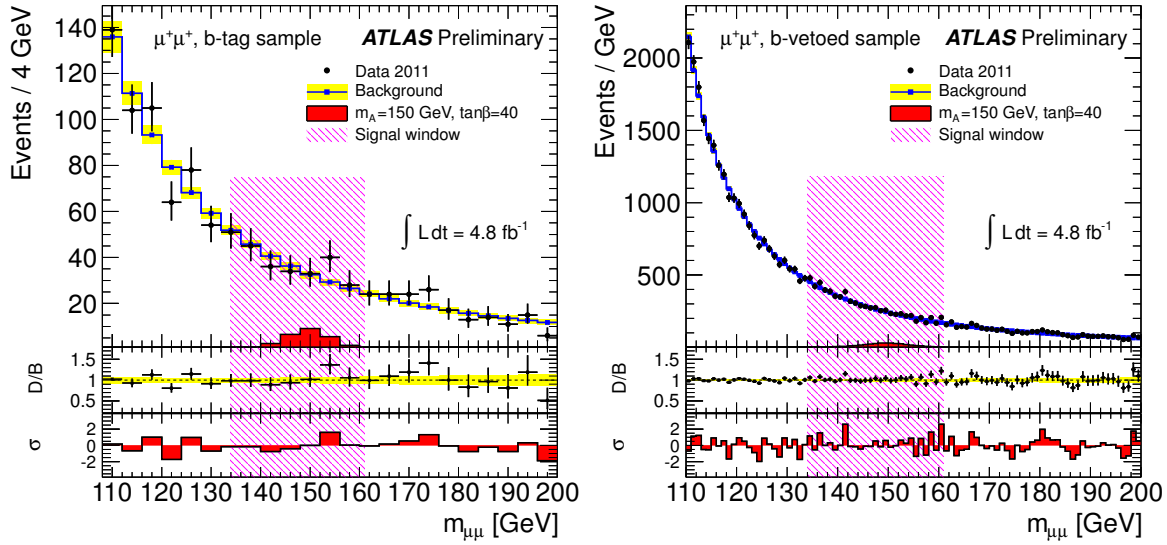

Figure 2: Invariant mass distribution (solid circles) and predicted background (blue) from sideband fits to the data shown for the signal mass point at $m_A = 150$ GeV and $\tan\beta = 40$ for the b-tagged (left-hand side) and the b-vetoed selections (right-hand side) of the $h/A/H \to \mu^+\mu^-$ final state. The insets labelled with D/B show the ratio of the data to the the predicted background. The insets labelled with σ show the bin-by-bin significances of the deviations of the data compared to the background prediction.

Signal modelling: The $h/A/H \to \mu^+\mu^-$ signal is expected to appear as a narrow resonance in the $\mu^+\mu^-$ invariant mass distribution. The resolution in the relevant mass range is typically 2.5 – 3 % and numerous mass points are needed for a complete mass scan. In addition, the influence of $\tan\beta$ on the reconstructed width of the signal invariant mass distribution needs to be taken into account. The natural width of the neutral MSSM Higgs bosons increases with $\tan\beta$. The reconstructed width can be sensitive to this variation because of the good experimental mass resolution.

To interpolate between the different resonances obtained from a limited number of simulated signal samples, the signal $\mu^+\mu^-$ invariant mass distribution is parameterised with

$$f_S(x, N, M, \Gamma, \sigma, c, \varsigma) = N\left[\frac{1}{[x^2 - M^2]^2 + M^2\Gamma^2} \otimes f_{Gauss}(x, \sigma) + c f_{Landau}(-x, M, \varsigma)\right], \qquad (3)$$

where x represents the running $\mu^+\mu^-$ invariant mass. The parameterisation consists of a Breit-Wigner function describing the signal peak convolved with a Gaussian distribution accounting for the finite mass resolution and a Landau function with left-hand side tail which models the asymmetric part of the signal invariant mass distribution.

Function f_S is characterised by six parameters. The width of the Breit-Wigner function, Γ, is fixed to its theoretical predictions calculated with FeynHiggs [28]. The remaining five parameters are free-floating. N is the overall normalization parameter and c specifies the relative normalization of the Landau function with respect to the Breit-Wigner function. The parameter M specifies the mean of the Breit-Wigner and the Landau distributions, σ determines the width of the Gaussian distribution and ς represents the scale parameter of the Landau function.

The function f_S is fit to each signal sample available from simulation. Each fit results in a set of fitted parameters, $(N, M, \sigma, c, \varsigma)$, depending on the point in the m_A–$\tan\beta$ plane. The distributions of

the five fit parameters are parameterised in m_{A} and $\tan\beta$ with polynomials of different orders. The resulting polynomials are used to interpolate between the limited number of simulated signal samples, thus providing a set of parameters which in addition to the predicted natural width, Γ, fully define the normalised probability density function for an arbitrary point in the m_{A}–$\tan\beta$ plane.

This procedure is used to generate invariant mass distributions for signal masses from 120–150 GeV in 5 GeV steps and from 150–300 GeV in 10 GeV steps, as well as for $\tan\beta$ values from 5–70 in steps of 3 or 5. For both the b-vetoed and b-tagged selections the interpolated normalised probability density functions are obtained separately for the Higgs boson production from gluon-fusion and in association with b quarks.

The resulting number of expected signal events in the fit range around the mass point $m_{\mathrm{A}} = 150$ GeV is given in Table 1 for both the b-vetoed and b-tagged selections, assuming the m_h^{max} scenario and $\tan\beta = 40$.

6 The $\tau^+\tau^-$ decay channel

The $h/A/H \to \tau^+\tau^-$ decay mode is analysed in several categories according to whether each τ lepton decays into an electron, a muon, or hadrons in addition to one or more neutrinos. The four decay modes considered here are: $\tau_{\mathrm{e}}\tau_{\mu}$, $\tau_{\mathrm{e}}\tau_{\mathrm{had}}$, $\tau_{\mu}\tau_{\mathrm{had}}$, $\tau_{\mathrm{had}}\tau_{\mathrm{had}}$. These decays have branching ratios of 6 % ($\tau_{\mathrm{e}}\tau_{\mu}$), 23 % ($\tau_{\mathrm{e}}\tau_{\mathrm{had}}$), 23 % ($\tau_{\mu}\tau_{\mathrm{had}}$), and 42 % ($\tau_{\mathrm{had}}\tau_{\mathrm{had}}$). The combination of $\tau_{\mathrm{e}}\tau_{\mathrm{had}}$ and $\tau_{\mu}\tau_{\mathrm{had}}$ is referred to as $\tau_{\mathrm{lep}}\tau_{\mathrm{had}}$.

6.1 Common background estimation and mass reconstruction techniques

τ-embedded $Z/\gamma^* \to \mu^+\mu^-$ data: $Z/\gamma^* \to \tau^+\tau^-$ events form a largely irreducible background to the Higgs boson signal in all selected final states. It is not possible to select a data-driven $Z/\gamma^* \to \tau^+\tau^-$ control sample which is Higgs signal-free. However, $Z/\gamma^* \to \mu^+\mu^-$ events can be selected in data with high purity and without significant signal contamination. Furthermore, the event topology and kinematics are, apart from the different masses of τ leptons and muons, identical to those of $Z/\gamma^* \to \tau^+\tau^-$ events. Therefore $Z/\gamma^* \to \mu^+\mu^-$ events are selected in data based on a single muon trigger and modified using the so-called embedding technique, which replaces the muons by simulated τ leptons. The hits of the muon tracks and the associated calorimeter cells in a cone of $\Delta R = 0.1$ around the muon direction are removed from the data event and replaced by the detector response of a simulated $Z/\gamma^* \to \tau^+\tau^-$ event with the same kinematics. The object and event reconstruction is performed on the combined event. Only the τ decays and the detector response are taken from the simulation, whereas the underlying event kinematics and the associated jets are taken from data.

The event yield of the embedded sample after the selection of the τ decay products is normalised to the corresponding event yield obtained in a simulated $Z/\gamma^* \to \tau^+\tau^-$ sample. This procedure has been extensively validated [58].

Jets misidentified as hadronic τ decays: A fraction of jets originating from quarks or gluons will have a signature such that they are misidentified as hadronic τ lepton decays. It has been shown in Reference [59] that this misidentification fraction is higher in simulated samples than in data. To account for this difference the Monte Carlo background estimate is corrected based on control samples in data for backgrounds in which the identified τ_{had} comes from a jet. Details are presented in the description of the analysis-specific background estimation.

The *ABCD* background estimation method: The so-called *ABCD* method is used for the estimation of the background from QCD multi-jet processes from data. Four independent samples are selected by using selection criteria on two variables. One of these regions is the signal region. The other three regions are independent control regions dominated by the background that is to be estimated. The regions obtained by inverting the criterion on one or the other of the two selected variables are labelled B and C. The region defined by simultaneously inverting the selection criteria on both variables is labelled D. If the two selected variables are uncorrelated for the background in question, the event yield n_A of this background in the signal region can be estimated by the event yield n_B in region B scaled by the ratio of event yields n_C and n_D in regions C and D:

$$n_A = n_B \times \frac{n_C}{n_D} \equiv n_B \times r_{C/D}. \tag{4}$$

For variables that are uncorrelated with the two used for the *ABCD* separation, the shape from any of the control regions can be used to model the distribution in the signal region.

To avoid biasing the estimated event yields and shapes, the remaining contributions from other backgrounds should be negligible or they have to be subtracted from the observed data events in the control regions.

$\tau^+\tau^-$ mass reconstruction: Due to the presence of neutrinos from the two τ decays, the reconstruction of the Higgs boson invariant mass requires special techniques. The simplest of these is the visible mass, defined as the invariant mass of the visible τ-decay products. Although the most probable value is not located at the nominal Higgs boson mass, it offers acceptable mass resolution while avoiding any dependence on the resolution of the measurement of missing transverse momentum.

A more sophisticated method is the Missing Mass Calculator (MMC) [60]. This algorithm tries to evaluate the most probable mass of the $\tau^+\tau^-$ system by deriving an approximate solution of the equations describing the Higgs boson decay into a $\tau^+\tau^-$ pair. Due to the unknown kinematics of the neutrinos escaping detection, these equations cannot be solved analytically. But, using the knowledge about simulated τ lepton decays, the measured missing transverse momentum, $E_{\mathrm{T}}^{\mathrm{miss}}$, and its known resolution, the most probable mass of the $\tau^+\tau^-$ system is evaluated instead.

The visible mass is used for the jet-vetoed $\tau_{\mathrm{e}}\tau_\mu$ decay channel, while all other decay channels use the MMC mass.

6.2 Analysis of the $h/A/H \to \tau_{\mathrm{e}}\tau_\mu$ decay channel

Signal topology and event selection: The preselection is applied to events containing electrons or muons: either a single electron trigger condition with a p_{T} threshold of 20 GeV or 22 GeV depending on the instantaneous luminosity, a combined electron-muon trigger condition with a p_{T} threshold of 10 GeV for the electron and 6 GeV for the muon, or a single muon trigger condition with a p_{T} threshold of 18 GeV must be fulfilled. Subsequently, exactly one isolated electron and one isolated muon of opposite electric charge, and with a di-lepton invariant mass above 30 GeV are required. If a single lepton trigger requirement is fulfilled, the p_{T} threshold applied to the corresponding reconstructed particle is raised from the one applied to all reconstructed electrons and muons to $p_{\mathrm{T}} > 24$ GeV for electrons and $p_{\mathrm{T}} > 20$ GeV in for muons. In order to further suppress events arising from di-boson production, $W \to \ell\nu$, and $t\bar{t}$ processes, the opening angle between the two lepton candidates in the transverse plane must satisfy the condition $\Delta\phi_{e\mu} > 2.0$.

The event sample is then split according to its jet content (using jets with $p_{\mathrm{T}} > 20$ GeV) to account for the two dominant Higgs boson production mechanisms in the MSSM, gluon-fusion and b-associated production.

Events containing an identified b jet enter the b-tagged selection. Events with an additional b jet are rejected to reduce the $t\bar{t}$ contribution. The working point of the flavour tagging algorithm provides a b jet tagging efficiency of 75 % in simulated $t\bar{t}$ events. A cut on the scalar sum of the lepton transverse momenta and missing transverse momentum, $E_{\mathrm{T}}^{\mathrm{miss}} + p_{\mathrm{T},e} + p_{\mathrm{T},\mu} < 125$ GeV, is applied to reduce top quark and di-boson backgrounds. In addition, the combination of the transverse opening angles between the lepton directions and the direction of $E_{\mathrm{T}}^{\mathrm{miss}}$ is required to satisfy the condition $\sum_{\ell=e,\mu} \cos\Delta\phi_{E_{\mathrm{T}}^{\mathrm{miss}},\ell} > -0.2$. Finally, the scalar sum of the transverse energies of all jets, H_{T}, is restricted to be below 100 GeV to further suppress backgrounds containing a higher multiplicity of jets, or jets with a higher transverse momentum, than expected from the signal processes. Reconstructed jets with $|\eta| < 4.5$ are used to calculate the value of H_{T}.

The jet-vetoed selection rejects events with jets fulfilling $p_{\mathrm{T}} > 20$ GeV, $|\eta| < 2.5$. A visible-mass window cut is applied; the optimal size and position for this window is chosen from Monte Carlo simulation for each mass hypothesis based on the expected discovery significance.

Estimation of the $Z/\gamma^* \to \tau^+\tau^-$ background: The shape of the $Z/\gamma^* \to \tau^+\tau^-$ background is estimated by using an embedded $Z/\gamma^* \to \mu^+\mu^-$ event sample as described in Section 6.1.

Estimation of the $t\bar{t}$ background: In the jet-vetoed selection, the $t\bar{t}$ background is small compared to the b-tagged selection. It is estimated using simulation in the jet-vetoed selection, while the contribution of $t\bar{t}$ production in the signal region of the b-tagged selection is extrapolated from a control region which has a purity of 90 %. The selection criteria for this control region are identical to the ones of the signal region with two exceptions: the veto on an additional identified b jet and the requirement of $H_{\mathrm{T}} < 100$ GeV are not applied. Instead, a second identified b jet with $p_{\mathrm{T}} > 20$ GeV is required.

The expected contribution of $t\bar{t}$ events in the resulting control region, $n_{\mathrm{CR}}^{t\bar{t}}$, is evaluated as the difference in the observed data events and the expected contributions from non-$t\bar{t}$ processes as predicted by simulation. The $t\bar{t}$ event yield in the control region is extrapolated into the signal region to estimate the contribution $n_{\mathrm{SR}}^{t\bar{t}}$ of $t\bar{t}$ processes passing the b-tagged selection:

$$n_{\mathrm{SR}}^{t\bar{t}} = K_{CR} \times n_{\mathrm{CR}}^{t\bar{t}}. \tag{5}$$

The extrapolation factor K_{CR} is derived by analysing $t\bar{t}$ events simulated with the MC@NLO and POWHEG Monte Carlo event generators. The values obtained for the two generators agree within statistical uncertainties. The shapes of the distributions in the signal region are obtained from a Monte Carlo prediction using MC@NLO.

Estimation of the multi-jet background: The multi-jet background for the jet-vetoed and b-tagged selections is estimated using an *ABCD* method as described in Section 6.1. The variables used to define the signal and control regions are the charge product of the selected leptons and the isolation requirements fulfilled by the leptons. Table 2 summarises the requirements imposed on these two variables in the signal region and the control regions.

The anti-isolated regions are dominated by multi-jet events, while contributions from other backgrounds are negligible. The same-sign isolated control region, B, contains sizable contributions from other processes. This contamination is subtracted from the observed number of data events according to the event yield predicted by simulation. The kinematic distributions for the multi-jet background in the signal regions are taken from control region B for the jet-vetoed selection. In the b-tagged selection the event yield in region B is insufficient for the extraction of the kinematic distributions, therefore control region C is used. Equation (4) is used to estimate the multi-jet background after the

Region	Charge correlation	Lepton isolation requirement
A (Signal Region)	Opposite sign	isolated
B	Same sign	isolated
C	Opposite sign	anti-isolated
D	Same sign	anti-isolated

Table 2: Control regions for the estimation of the multi-jet background for the $h/A/H \to \tau_{\mathrm{e}}\tau_{\mu}$ and $h/A/H \to \tau_{\mathrm{lep}}\tau_{\mathrm{had}}$ selections: Events are categorised according to the product of the electric charges of the electron and the muon ($h/A/H \to \tau_{\mathrm{e}}\tau_{\mu}$ selection) and the electron or muon and the reconstructed τ lepton ($h/A/H \to \tau_{\mathrm{lep}}\tau_{\mathrm{had}}$ selection) and according to the lepton isolation requirement. In the $h/A/H \to \tau_{\mathrm{lep}}\tau_{\mathrm{had}}$ channel isolation refers to the isolation of the electron or muon and in the $h/A/H \to \tau_{\mathrm{e}}\tau_{\mu}$ channel both the electron and muon are required to be isolated or anti-isolated respectively.

b-tagged selection, as well as for each $m_{e\mu}$ mass window of the jet-vetoed selection from the respective set of control regions.

Results: Figure 3 shows the distributions of the variables used to derive the final results after the full selection in the two channels. A signal hypothesis of $m_A = 150$ GeV and $\tan\beta = 20$ is included. The corresponding event yields are shown in Table 3. The results for the jet-vetoed selection in this table are shown for the signal window optimised for the mass point $m_A = 150$ GeV.

6.3 Analysis of the $h/A/H \to \tau_{\mathrm{lep}}\tau_{\mathrm{had}}$ decay channel

Signal topology and event selection: Events in the $h/A/H \to \tau_{\mathrm{lep}}\tau_{\mathrm{had}}$ channel are selected using a single-lepton trigger with transverse momentum thresholds of 20 GeV or 22 GeV for electrons and 18 GeV for muons and must contain one isolated electron with $p_{\mathrm{T}} > 25$ GeV or one isolated muon with $p_{\mathrm{T}} > 20$ GeV. Events containing additional electrons or muons with transverse momenta greater than 15 GeV or 10 GeV, respectively, are rejected in order to obtain an orthogonal selection to the $h/A/H \to \tau_{\mathrm{e}}\tau_{\mu}$ and $h/A/H \to \mu^{+}\mu^{-}$ channels. One τ jet with a charge of opposite sign to the selected electron or muon is required. The τ_{had} identification criteria used correspond to a τ_{had} identification efficiency of about 45 % (see also Section 4). The transverse mass, m_{T}, between the lepton and the missing transverse momentum, $E_{\mathrm{T}}^{\mathrm{miss}}$, is defined as:

$$m_{\mathrm{T}} = \sqrt{2 p_{\mathrm{T}}^{\mathrm{lep}} E_{\mathrm{T}}^{\mathrm{miss}} \left(1 - \cos\Delta\phi\right)}\,, \tag{6}$$

where $p_{\mathrm{T}}^{\mathrm{lep}}$ denotes the transverse momentum of the electron or muon and $\Delta\phi$ the angle between the lepton and $E_{\mathrm{T}}^{\mathrm{miss}}$ in the plane perpendicular to the beam direction. Events are required to satisfy $m_{\mathrm{T}} < 30$ GeV to reduce contamination from W + jets and $t\bar{t}$ background processes.

After these baseline selection criteria the resulting event sample is split depending on whether or not the highest-p_{T} jet in the event is identified as a b jet. For the b jet identification a working point with a 70 % identification efficiency measured in simulated $t\bar{t}$ events is used. Events pass the b-tagged selections if the highest-p_{T} jet is identified as a b jet and its p_{T} is in the range from 20 GeV to 50 GeV. Events pass the b-vetoed selection if the highest-p_{T} jet fails the b jet identification criterion and if $E_{\mathrm{T}}^{\mathrm{miss}} > 20$ GeV.

	b-tagged selection	Jet-vetoed selection
$Z/\gamma^* \to \tau^+\tau^-$	$109\pm5\ ^{+11}_{-10}$	$685\pm14\ ^{+85}_{-74}$
W + jets	$1.17\pm0.83^{+0.66}_{-0.19}$	$47\pm11\ ^{+5}_{-6}$
$Z/\gamma^* \to \ell^+\ell^-$	$1.07\pm0.76^{+0.16}_{-0.13}$	$45.9\pm5.1^{+4.1}_{-3.6}$
$t\bar{t}$	$54.3\pm5.7\ ^{+9.1}_{-6.7}$	$23.4\pm0.9^{+3.9}_{-4.2}$
Single top	$15.7\pm1.2\ ^{+2.4}_{-3.9}$	$11.9\pm1.0\pm1.5$
Di-boson	$3.91\pm0.37^{+0.60}_{-0.55}$	$325\pm3\ ^{+30}_{-31}$
Multi-jet	$15\pm11\ \pm2$	$60\pm12\ ^{+9}_{-6}$
Total	$200\pm13\ ^{+15}_{-13}$	$1197\pm22\ ^{+91}_{-80}$
$b\bar{b}h/A/H \to \tau\tau$	$18.8\pm0.6\ ^{+4.2}_{-5.2}$	$105\pm6\ ^{+12}_{-16}$
$gg \to h/A/H \to \tau\tau$	$2.60\pm0.31^{+0.75}_{-0.76}$	$41.6\pm5.9^{+6.4}_{-6.3}$
Data	181	1245

Table 3: The number of events observed in data and the expected number of signal and background events for the signal regions of the $h/A/H \to \tau_e\tau_\mu$ channel. Simulated event yields are normalised to the integrated luminosity of the data sample, 4.7 fb^{-1}. In the jet-vetoed sample the requirements on the visible mass depend on the Higgs boson mass hypothesis. The selection shown requires 70 GeV $< m_{e\mu} <$ 120 GeV, to optimise the sensitivity for a Higgs-boson mass of m_A = 150 GeV. The predicted signal event yields correspond to a parameter choice of m_A = 150 GeV and $\tan\beta$ = 20 and include both the b-associated and the gluon-fusion production processes. The statistical and systematic uncertainties on the expectations are shown.

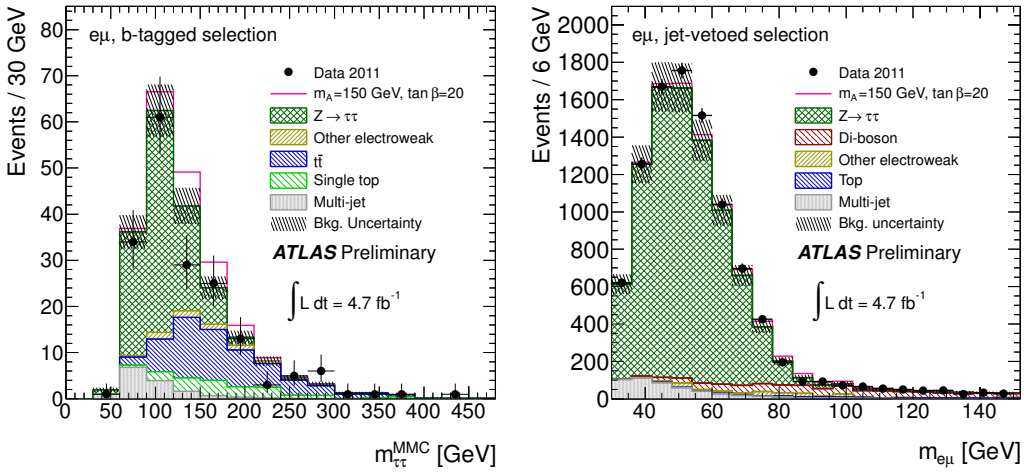

Figure 3: Final mass distributions for the $h/A/H \to \tau_e\tau_\mu$ final state. The observable for the b-tagged selection (left-hand side) is the MMC mass, (m_{MMC}). The background contribution from top quark productions is shown individually for $t\bar{t}$ and single top production for the $h/A/H \to \tau_e\tau_\mu$ + b-tag channel, to distinguish between background estimates from data and from Monte Carlo simulation. For the jet-vetoed selection (right-hand side) the invariant mass of the selected leptons, $m_{e\mu}$, is used. The data are compared to the background expectation and an added hypothetical MSSM signal with $m_{\mathrm{A}} = 150$ GeV and $\tan\beta = 20$. The background uncertainties include statistical and systematic uncertainties.

Estimation of the W + jets background: W + jets events that pass the event selection up to the m_{T} requirement consist primarily of events in which the selected lepton originates from the W decay and a jet is misidentified as a τ jet. To ensure a proper estimation of the jet-to-τ misidentification rate, the W + jets background normalisation is corrected using control regions defined by requiring high transverse mass: 70 GeV $< m_{\mathrm{T}} <$ 110 GeV. Separate control regions are used for the $\tau_e\tau_{\mathrm{had}}$ and $\tau_\mu\tau_{\mathrm{had}}$ samples. The purity of W + jets events for these control regions is above 80 %. Correction factors are derived using the expression

$$f_W^\ell = \frac{n_{\mathrm{data}}^{\mathrm{CR}} - n_{\mathrm{rest\ MC}}^{\mathrm{CR}}}{n_{\mathrm{W\ MC}}^{\mathrm{CR}}}, \tag{7}$$

where $n_{\mathrm{data}}^{\mathrm{CR}}$ is the number of events observed in data, and $n_{\mathrm{W\ MC}}^{\mathrm{CR}}$ and $n_{\mathrm{rest\ MC}}^{\mathrm{CR}}$ are the estimates for the number of W + jets events and events due to other background processes. With this definition, the correction factors derived are $f_W^e = 0.587 \pm 0.009$ for the electron channel and $f_W^\mu = 0.541 \pm 0.008$ for the muon channel, where the quoted uncertainty is statistical. The requirement of a b-tagged jet in the final state has a small effect on these correction factors, which is treated as an additional systematic uncertainty and is described in Section 7.2.

Estimation of the $Z/\gamma^* \to \tau^+\tau^-$ background: The shape of the $Z/\gamma^* \to \tau^+\tau^-$ background is estimated using the τ-embedded $Z/\gamma^* \to \mu^+\mu^-$ sample described in Section 6.1.

The jet activity in the embedded events is independent of the Z boson decay mode. By taking advantage of this feature, the embedding sample is also used to validate the simulated $Z/\gamma^* \to e^+e^-$ and $Z/\gamma^* \to \mu^+\mu^-$ background samples for the correct b jet fraction, which may affect the background estimation after imposing the b-tag requirement. Correction factors are derived by comparing τ-

embedded $Z/\gamma^* \to \mu^+\mu^-$ events with simulated $Z/\gamma^* \to \tau^+\tau^-$ events before and after the b-tagged selection criterion. The correction factors are calculated to be $f^e_{Z,b} = 1.08 \pm 0.23$ and $f^\mu_{Z,b} = 1.11 \pm 0.13$ for the electron and muon channels, respectively.

Estimation of the $t\bar{t}$ background: Simulation shows that a significant fraction of the selected τ_{had} candidates in the $t\bar{t}$ events passing the event selection are misidentified jets. To account for a possible difference in the normalisation of the simulated samples, a correction factor for $t\bar{t}$ events is derived from a control region. The baseline selection criteria are applied for this control region, but the requirement on m_{T} is dropped in order to enhance the fraction of $t\bar{t}$ events. The leading jet must be tagged as a b jet and its transverse momentum is required to be within the range of 50–150 GeV. In addition, a second jet must pass the same b-tag requirements as the leading jet. This results in a control region with a purity of $t\bar{t}$ events over 90 %. The signal yield in the control region can be neglected. The $t\bar{t}$ correction factor is derived in a manner similar to that of the W + jets correction factor and a value of $f_{t\bar{t}} = 0.88 \pm 0.04$ is obtained where the quoted uncertainty is statistical.

Estimation of the multi-jet background: The multi-jet background is estimated using the *ABCD* method as described in Section 6.1. The event sample is split according to whether the charge of the τ jet and lepton have opposite sign (OS) or same sign (SS), and whether the selected lepton passes or fails the isolation criterion. The region obtained by demanding SS and the lepton passing the isolation requirement is referred to as region *B*. The region obtained by demanding OS and the lepton failing the isolation requirement is called region *C*. Region *D* is defined by demanding both SS and the lepton failing the isolation requirement. These definitions are also shown in Table 2.

In regions *C* and *D* the contribution from processes other than the multi-jet background is negligible. In region *B* there is a significant contribution from other backgrounds, in particular Z/γ^*+jets and W + jets, which are subtracted from the data sample using estimates from simulation. The contamination from potential signal processes in any of the control regions is negligible. The final estimate of the multi-jet background yield in data is calculated using Equation (4).

Results: Table 4 shows the number of events observed in data and the expected event yields from signal and background processes. The final results are derived from the di-τ mass distribution calculated with the MMC algorithm. The distribution of the MMC mass can be seen in Figure 4, with the $\tau_{\text{e}}\tau_{\text{had}}$ and $\tau_\mu\tau_{\text{had}}$ channels combined.

6.4 Analysis of the $h/A/H \to \tau_{\text{had}}\tau_{\text{had}}$ decay channel

Signal topology and event selection: The signal in this decay channel is characterised by two τ_{had} and modest missing transverse momentum. In addition, b jets may be produced due to the b-associated Higgs boson production process. Events are preselected by a di-τ_{had} trigger with transverse momentum thresholds of 29 GeV and 20 GeV for the two candidates. Events containing identified electrons or muons with transverse momenta above 15 GeV or 10 GeV, respectively, are vetoed. These vetoes suppress background events with an electron or muon and assure orthogonality to the other channels. Two τ jet candidates with opposite-sign charges are required, one passing the requirements for the tighter optimisation of the τ_{had} identification and the second passing the intermediate one. The identification optimisations correspond to identification efficiencies of approximately 35 % and 45 %. This combination represents a good compromise between signal efficiency and background rejection and provides control samples sufficiently large for the background estimates described in the sections

	Muon Channel	
	b-tagged selection	b-vetoed selection
$Z/\gamma^* \to \tau^+\tau^-$	86±7 ±13	4760±50 ±740
W + jets	$19.4\pm3.9\ ^{+5.2}_{-6.7}$	$780\pm30\ ^{+100}_{-140}$
$Z/\gamma^* \to \ell^+\ell^-$	$8.3\pm2.3\ ^{+4.5}_{-3.4}$	$351\pm16\ ^{+98}_{-93}$
Top	$14.5\pm0.8\ ^{+3.4}_{-2.6}$	$105\pm2\ ^{+20}_{-21}$
Di-boson	$0.75\pm0.33^{+0.23}_{-0.18}$	$37.5\pm1.9^{+5.2}_{-4.3}$
Multi-Jet	$50.5\pm8.8\ ^{+6.9}_{-5.6}$	$580\pm50\ ^{+130}_{-120}$
Total	$180\pm12\ ^{+17}_{-16}$	$6610\pm70\ ^{+760}_{-770}$
$b\bar{b}h/A/H \to \tau\tau$	$20.4\pm1.4\ ^{+4.6}_{-6.1}$	$174\pm4\ ^{+27}_{-35}$
$gg \to h/A/H \to \tau\tau$	$1.20\pm0.38^{+0.53}_{-0.36}$	$115\pm4\ ^{+15}_{-16}$
Data	202	6424

	Electron Channel	
	b-tagged selection	b-vetoed selection
$Z/\gamma^* \to \tau^+\tau^-$	42±6 ±19	$2730\pm50\ ^{+480}_{-490}$
W + jets	$18.3\pm8.3\ ^{+4.9}_{-8.5}$	$740\pm20\ ^{+110}_{-160}$
$Z/\gamma^* \to \ell^+\ell^-$	$18.8\pm4.1\ ^{+8.7}_{-9.1}$	$700\pm20\ ^{+350}_{-270}$
Top	$15.1\pm0.8\ ^{+2.9}_{-2.7}$	$106\pm2\ ^{+20}_{-21}$
Di-boson	$0.95\pm0.35^{+0.14}_{-0.32}$	$29.3\pm1.7^{+4.6}_{-4.3}$
Multi-Jet	60±9 ±12	$920\pm50\ ^{+220}_{-230}$
Total	$154\pm14\ ^{+25}_{-26}$	$5220\pm80\ ^{+640}_{-620}$
$b\bar{b}h/A/H \to \tau\tau$	$15.0\pm1.2\ ^{+3.0}_{-4.8}$	$138\pm4\ ^{+22}_{-29}$
$gg \to h/A/H \to \tau\tau$	$1.20\pm0.40^{+0.50}_{-0.23}$	$99\pm3\ ^{+15}_{-14}$
Data	175	5034

Table 4: The number of events observed in data and the expected number of signal and background events for the signal regions of the $h/A/H \to \tau_{\text{lep}}\tau_{\text{had}}$ channel. Simulated event yields are normalised to the integrated luminosity of the data sample, 4.7 fb^{-1}. The predicted signal event yields correspond to the parameter choice $m_A = 150$ GeV and $\tan\beta = 20$ and include both the b-associated and the gluon-fusion production processes. The statistical and systematic uncertainties on the expectations are shown.

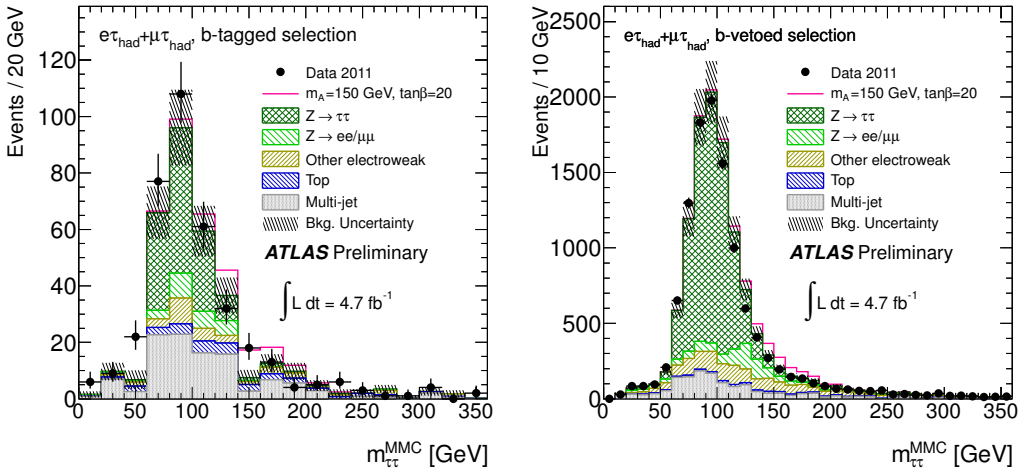

Figure 4: Final mass distributions for the $h/A/H \rightarrow \tau_{\text{lep}}\tau_{\text{had}}$ final state. The MMC mass is shown for the b-tagged (left-hand side) and b-vetoed selections (right-hand side) for the combined $\tau_{\text{e}}\tau_{\text{had}}$ and $\tau_{\mu}\tau_{\text{had}}$ samples. The data are compared to the background expectation and a hypothetical MSSM signal with $m_{\text{A}} = 150$ GeV and $\tan\beta = 20$. The background uncertainties include statistical and systematic uncertainties.

that follow. The two leading τ jet candidates are required to match the reconstructed τ jet trigger objects within a cone of $\Delta R < 0.2$. The two τ jet candidates are required to have visible transverse momenta above 45 GeV and 30 GeV, respectively. These thresholds are chosen such that the plateau of the trigger turn-on curve is reached, and electroweak and multi-jet backgrounds are suppressed effectively. The missing transverse momentum is required to be above 25 GeV to account for the presence of neutrinos originating from the τ decays, and to suppress multi-jet background.

The selected event sample is split using a b-tagged and a b-vetoed selection to exploit the two Higgs boson production mechanisms in the MSSM. Events in which the leading jet is identified as a b jet pass the b-tagged selection. The identification is based on a b-tagging algorithm with an identification efficiency of 70 % in simulated $t\bar{t}$ events. The transverse momentum of this jet is restricted to the range of 20–50 GeV to reduce the $t\bar{t}$ background. Events without jets, or in which the leading jet is not identified as a b jet, pass the b-vetoed selection. Due to the higher background in this sample, the threshold on the visible transverse momentum of the leading τ jet candidate is raised to 60 GeV. The MMC mass is used as a final mass estimator for the b-tagged and b-vetoed selections.

Efficiency and misidentification corrections for hadronic τ decays: The τ_{had} identification efficiencies, the τ_{had} trigger efficiencies and the corresponding misidentification probabilities are corrected for differences observed between data and simulation.

For the di-τ_{had} trigger it is assumed that these identification and misidentification efficiencies can be factorised into the efficiencies of the corresponding single-τ_{had} triggers with appropriate transverse momentum requirements. This factorisation is validated using a simulated event sample. The single-τ_{had} trigger efficiency for real τ leptons with respect to the offline τ_{had} selection was measured in data using a tag-and-probe analysis with $Z \rightarrow \tau_{\mu}\tau_{\text{had}}$ data and correction factors for the simulation were derived as a function of the transverse momenta of the two τ jet candidates. The probability to misidentify a jet as a τ jet is extracted for both the trigger and the τ_{had} identification algorithm by

Region	Charge correlation	hadronic τ decay identification requirement
A (Signal Region)	Opposite sign	pass tight and medium
B	Same sign	pass tight and medium
C	Opposite sign	fail tight and medium
D	Same sign	fail tight and medium

Table 5: Control regions for the estimation of the multi-jet background for the $h/A/H \to \tau_{\text{had}}\tau_{\text{had}}$ selection: Events are categorised according to the product of the electric charges of the two hadronic τ decays and the hadronic τ decay identification requirement. Pass tight and medium refers to one τ decay passing the tighter identification requirements and the other decay passing at least the intermediate identification requirements. Fail tight and medium refers to two classes of events. In the first class of events one τ decay passes the tighter identification requirements and the second τ decay only passes the looser requirements but not the intermediate ones. In the second class of events none of the two τ decays pass the tighter identification criteria but both pass the intermediate or the looser ones.

analysing jets in a high-purity $W(\to \mu\nu)$+jets sample. A correction factor derived on the basis of these probabilities is applied to the simulation when a jet is misidentified as a τ_{had} .

Estimation of the $Z/\gamma^* \to \tau^+\tau^-$ and $W(\to \tau\nu)$+jets backgrounds: The estimates of the $Z/\gamma^* \to \tau^+\tau^-$ and $W(\to \tau\nu)$+jets backgrounds are taken from simulation. As a validation of the predictions from simulation, the shapes of the simulated distributions of important variables are compared with the ones obtained from a τ-embedded $Z/\gamma^* \to \mu^+\mu^-$ sample.

The $Z/\gamma^* \to \tau^+\tau^-$ and $W(\to \tau\nu)$+jets backgrounds are studied using τ-embedded $Z/\gamma^* \to \mu^+\mu^-$ and $W(\to \mu\nu)$+jets data samples as described in Section 6.1.

Correction factors for the efficiency of the b-tagging requirement on the leading jet are derived in a way equivalent to that described in Section 6.3. For the Z/γ^* + jets background the factor is derived by comparing the simulated and embedded $Z/\gamma^* \to \tau^+\tau^-$ samples. A correction factor of $f_{Zb} = 1.24 \pm 0.34$ is obtained for the selection applied in this channel. With the embedded $W(\to \tau\nu)$+jets sample, no correction factor can be derived in such a way since the contamination from $t\bar{t}$ events is quite significant once the b-tag requirements are applied. Instead, the procedure in Section 6.3 is applied with the baseline selection of this channel. A correction factor of $f_{Wb} = 1.00 \pm 0.31$ is derived for $W(\to \tau\nu)$+jets events. The correction factors for the b-vetoed selection are found to be compatible with unity, within uncertainty, and no correction is applied.

Estimation of the multi-jet background: The multi-jet background is estimated using the $ABCD$ method as described in Section 6.1. The event samples are split into four regions based on the charge product of the two leading τ jet candidates, i.e. opposite-sign or same-sign charges and whether the nominal τ_{had} identification requirements of these two τ jet candidates are met. To a good approximation, these variables can be assumed to be uncorrelated for multi-jet events.

The signal region A is the region in which the two τ jet candidates with opposite-sign charges satisfy the nominal τ_{had} identification requirements. In region B the two τ jet candidates must satisfy the same identification requirements but are required to have same-sign charges. In regions C and D at least one of the two τ jet candidates must fail the nominal τ_{had} identification requirement, but pass a looser selection (see Table 5). In region C the two candidates must have opposite-sign charges, in region D same-sign charges. Table 5 illustrates the definition of these four regions.

The contribution from electroweak backgrounds in the control regions B, C, and D is small. This

amounts to ~ 10 % in region B and ~ 5 % in regions C and D. The electroweak background contribution is subtracted from the observed data in each control region. The shape of the distribution of the MMC mass for the multi-jet background in the signal region is taken from region C for the b-vetoed selection and from region B for the b-tagged selection.

Using the observed and expected numbers of events in the control regions, together with Equation (4), the contribution of multi-jet background in the signal region is estimated to be 19.3 ± 4.6 events after the b-tagged selection, and 867 ± 21 events after the b-vetoed selection.

All other backgrounds have been estimated from simulation.

Results: A total of 27 events are observed in the data after the b-tagged selection and 1223 events remain in data after the b-vetoed selection. These numbers are consistent with the expected number of events after the b-tagged and b-vetoed selections, $25.4 \pm 4.8\,^{+2.2}_{-1.9}$ and $1232 \pm 23\,^{+68}_{-59}$, respectively. Table 6 shows the composition of the selected samples and the expected signal yields for $m_{\mathrm{A}} = 200$ GeV and $\tan\beta = 20$.

The final discriminating variable used to look for a potential signal contribution from a neutral MSSM Higgs boson is the MMC mass, m_{MMC}. The m_{MMC} distribution after each of the b-vetoed and the b-tagged selections are shown in Figure 5.

	b-tagged selection	b-vetoed selection
Multi-jet	$19.3 \pm 4.6\,^{-1.1}_{+1.3}$	$867 \pm 21\,^{-40}_{+39}$
$Z/\gamma^* \rightarrow \tau^+\tau^-$ + jets	$4.0 \pm 1.2\,^{+2.8}_{-2.6}$	$298 \pm 8\,^{+80}_{-66}$
W + jets	$0.51 \pm 0.37\,^{+0.27}_{-0.16}$	$52 \pm 5\,^{+16}_{-20}$
Top	$1.65 \pm 0.25 \pm 0.45$	$11.2 \pm 0.7 \pm 2.0$
Di-boson	$0.013 \pm 0.035 \pm 0.009$	$4.86 \pm 0.46 \pm 0.90$
Total	$25.4 \pm 4.8\,^{+2.2}_{-1.9}$	$1233 \pm 23\,^{+69}_{-59}$
$b\bar{b}h/A/H \rightarrow \tau\tau$	$7.7 \pm 0.6\,^{+3.3}_{-3.2}$	$73 \pm 2\,^{+21}_{-20}$
$gg \rightarrow h/A/H \rightarrow \tau\tau$	$0.50 \pm 0.18\,^{+0.04}_{-0.13}$	$47 \pm 2\,^{+11}_{-10}$
Data	27	1223

Table 6: The observed number of events in data and the expected number of signal and background events for the signal regions for the $h/A/H \rightarrow \tau_{\mathrm{had}}\tau_{\mathrm{had}}$ channel. Simulated event yields are normalised to the total integrated luminosity, 4.7 fb^{-1}. The predicted signal event yields correspond to the parameter choice $m_A = 150$ GeV and $\tan\beta = 20$ and include both the b-associated and gluon-fusion production processes. The statistical and systematic uncertainties on the expectations are shown.

7 Systematic uncertainties

In this search, the event yields and the mass distributions have been estimated using data-driven control samples and Monte Carlo simulation. Uncertainties related to simulation, such as reconstruction effects and event generation are presented in Section 7.1. Uncertainties on data-driven background estimations for the $\tau^+\tau^-$ and the $\mu^+\mu^-$ decay channels are discussed in Section 7.2

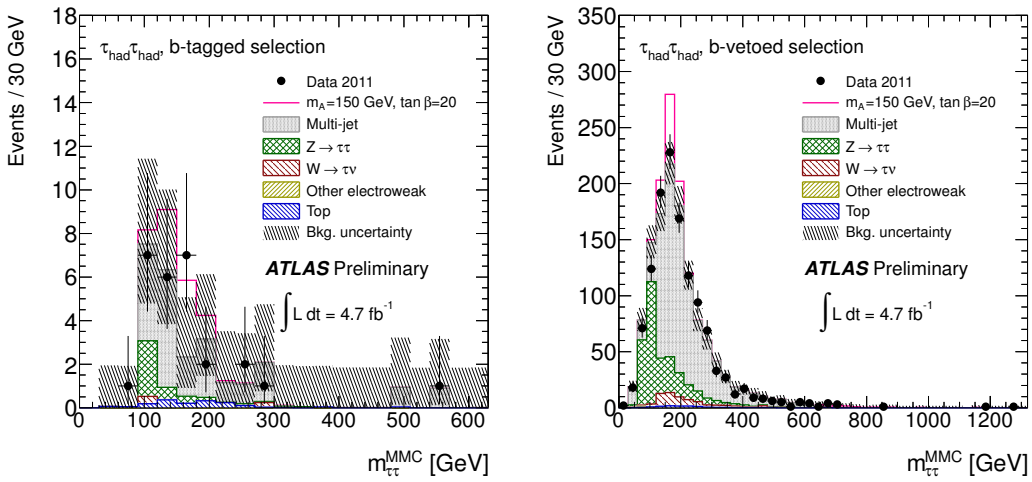

Figure 5: Final mass distributions for the $h/A/H \to \tau_{\text{had}}\tau_{\text{had}}$ final state. The MMC mass is shown for the b-tagged (left-hand side) and b-vetoed selections (right-hand side). The data are compared to the background expectation and an added hypothetical MSSM signal with $m_{\text{A}} = 150$ GeV and $\tan\beta = 20$). The background uncertainties include statistical and systematic uncertainties.

7.1 Systematic uncertainties for simulated samples

Cross sections for signal and background simulated samples: The uncertainties on the signal cross sections depend on m_A and $\tan\beta$ and lie in the range of $10 - 20\,\%$ for both gluon-fusion and b-associated Higgs boson production [29]. Uncertainties due to the parton distribution functions (PDF) and the renormalisation and factorisation scales are included.

Systematic uncertainties related to the parameters used in the event generation of signal and background samples are evaluated by varying the relevant scale parameters, PDF choices and, if applicable, conditions for the matching of the partons used in the fixed order calculation and the parton shower. Furthermore, the effects of different tunes of the underlying event activity have been studied.

Electron, muon and hadronic τ decay identification and trigger: The electron identification efficiency correction factors in the range from 0.87 to 0.99 (depending on η and p_{T}) are obtained with relative uncertainties of $3 - 6\,\%$ [47]. The main reason for the deviation from unity is due to the mismodeling of tight isolation conditions in the simulation.

The muon identification efficiency correction factors are consistent with unity within their 1.8 % relative uncertainties [48, 61]. Uncertainties on the τ_{had} identification efficiency are 4 % for all hadronic τ decays with p_T above 22 GeV and 8 % for those with p_T below 22 GeV [55]. Uncertainties on the probability for an electron to be misidentified as a hadronic τ decay have been evaluated and found to be in the range of $30 - 100\,\%$, depending on the η region.

Electron and muon trigger efficiency correction factors are calculated from data using $Z \to ee$ and $Z \to \mu\mu$ events. The correction factor uncertainty is up to about 1 %.

In the $\tau_{\text{had}}\tau_{\text{had}}$ channel, p_{T}-dependent trigger efficiency correction factors are determined from data using $Z/\gamma^* \to \tau^+\tau^-$ and $W(\to \tau\nu)$+jets events. These uncertainties result in systematic uncertainties on the acceptance in the range of $0.5 - 5\,\%$ for the various signal and background samples.

***b*-jet identification uncertainties:** The identification of a b jet also contributes to the total uncertainty and has been studied in detail in References [62, 63]. Uncertainties on the (mis-)identification of jets from b quarks, c quarks, and other partons are considered. The effect of these uncertainties is about 4–10 % for signal and up to 30 % for background samples for the b-tagged selection and up to about 1 % for signal and 10 % for background samples for the b-vetoed selection. The effect of this systematic uncertainty is highly reduced due to the fact that the embedded samples are used to model the $Z \to \tau^+\tau^-$ background.

Energy scale and resolution: The acceptance change due to the energy measurement in the calorimeter is considered for each identified object corresponding to the clusters of the calorimeters. For the clusters identified as electrons, typically a 1 % (3 %) energy scale uncertainty is assigned for the barrel (end-cap) region. The energy scale uncertainties for clusters identified as hadronic τ decays and jets are treated as being fully correlated. The typical energy scale uncertainty is around 3 % for both hadronic τ decays [64] and jets [52]. The acceptance changes due to the energy scale are assigned as jet and τ energy scale uncertainties for each background component. The acceptance uncertainty due to the jet energy resolution, which affects the p_T thresholds used to define the jet-vetoed, b-tagged, and b-vetoed selections, is typically < 1 %. The systematic uncertainty due to the energy scales of electrons, muons, hadronic τ decays and jets, is propagated to the $E_{\mathrm{T}}^{\mathrm{miss}}$ vector. For the $Z/\gamma^* \to \tau^+\tau^-$ embedding, energy scale uncertainties are considered with the exception of those applied to jets, as the jets in the sample are taken directly from collision data. Additional uncertainties due to different pile-up conditions in data and simulation are also studied.

7.2 Systematic uncertainties for data-driven methods

Systematic uncertainties for the τ-embedded $Z/\gamma^* \to \mu^+\mu^-$ sample: Systematic uncertainties on the normalization and shape of the τ-embedded $Z/\gamma^* \to \mu^+\mu^-$ sample are derived by varying the details of the treatment of calorimeter cells close to the muon. The isolation requirement imposed on the muons to get a clean sample of $Z/\gamma^* \to \mu^+\mu^-$ events could potentially bias the energy measurement of the visible decay products of the simulated τ lepton that has replaced it. To estimate this effect, samples were produced with the isolation requirement removed or tightened; the resulting event yields vary by a few percent, depending on the channel. Furthermore, the calorimeter energy that is subtracted for each muon is varied by ±30 %, to account for a possible inaccurate estimation of the amount of energy deposited by muons traversing the calorimeter. The effect on the event yields is on the order of a few percent. Finally, because the normalization of the embedding sample is determined by the theoretical cross section and acceptance, additional uncertainties are assigned on the normalization. These uncertainties are described in detail in Section 7.1.

Systematic uncertainties for the data-driven methods used in the $\tau_e\tau_\mu$ decay channel: The multi-jet background estimate, based on the *ABCD* method, as described in Section 6.2, carries a systematic uncertainty on the expected event yield from possible correlations of the variables used. The uncertainty on the normalization can be assessed by comparing $r_{C/D}$, the ratio of events with non-isolated leptons with opposite charge to non-isolated leptons with same charge, for different isolation requirements. The resulting systematic uncertainty on the event yield has been found to be negligible for the jet-vetoed selection, and 14 % for the b-tagged selection. For the b-tagged selection, the uncertainty due to possible correlations between m_{MMC} and the isolation variables is estimated by comparing the m_{MMC} distribution for a control region where both oppositely-charged leptons are non-isolated and a control region with oppositely-charged leptons where the muon is non-isolated and the

electron is isolated. For the jet-vetoed selection correlations between the visible mass and the charge product of the leptons are negligible.

For the $t\bar{t}$ contribution to the b-tagged selection, the uncertainty of the extrapolation factor K_{CR} is estimated by considering the object-related uncertainties described in Section 7.1, with the b-tagging efficiency and jet energy scale uncertainties being the dominant sources of uncertainty. The final value has a systematic uncertainty of $^{+17}_{-12}$ %. In the jet-vetoed selection, event yields are obtained from the Monte Carlo prediction.

Systematic uncertainties for the data-driven methods used in the $\tau_{\text{lep}}\tau_{\text{had}}$ decay channel: The multi-jet background estimate, based on the *ABCD* method and described in Section 6.3, has an uncertainty of 7.5 % in the muon channel and 15 % in the electron channel due to the instability of the $r_{C/D}$ ratio across the m_{MMC} range and variations in the definitions of the regions used. Smaller effects from the uncertainties on the subtracted Monte Carlo backgrounds are also considered. The $t\bar{t}$ normalization, estimated from a control region with high m_T and two b-tagged jets, has an uncertainty of 14.5 % from the b jet identification efficiency and 5.7 % from varying the m_T and b jet p_{T} thresholds as defined for the control region. The correction factors for the W + jets background, described in 6.3, have been assigned a 5 % systematic uncertainty arising from variations in the m_T boundary definition of the control region. The same correction factors are used for the b-tagged selection, but with an uncertainty of 17 %, due by the $t\bar{t}$ cross section uncertainty and the differences of the correction factors before and after the b-tagged selection requirements in the control region. The correction factors for the $Z/\gamma^* \to e^+e^-$ and $Z/\gamma^* \to \mu^+\mu^-$ backgrounds after the b-tagged selection $f^e_{Z,b}$ and $f^\mu_{Z,b}$ are found to have a dependence on the jet p_T threshold that is applied in the b-tagged selection. The effect of this jet p_T cut is 7 % and it is assigned as a systematic uncertainty on the correction factors.

Systematic uncertainties for the data-driven methods used in the $\tau_{\text{had}}\tau_{\text{had}}$ decay channel: The statistical uncertainties associated with the method used to determine the probability for the misidentification of jets as τ_{had} candidates, described in Section 6.4, lead to systematic uncertainties of 21 % on the W + jets background estimate and less than 1 % on the other backgrounds for both the b-tagged and the b-vetoed selections. A 4 % systematic uncertainty on the $t\bar{t}$ background is obtained for the b-tagged selection, and 6 % on the $t\bar{t}$ background for the b-vetoed selection. Correction factors have been determined for the W + jets and Z/γ^* + jets backgrounds in the b-tagged analysis to remediate the observed difference in the efficiency of the b jet requirement in data compared to Monte Carlo simulation. The uncertainty on these factors results in a systematic uncertainty of 31 % and 34 % on the W + jets and Z/γ^* + jets backgrounds, respectively. The systematic uncertainty on the multi-jet background is evaluated by varying the contributions of the electroweak backgrounds, which need to be subtracted from the expectations in the control regions, within their uncertainties. The total systematic uncertainty on the multi-jet background is $^{+7}_{-6}$ % for the b-tagged selection and ±5 % for the b-vetoed selection.

8 Statistical analysis

The statistical analysis of the data employs a binned likelihood function constructed as the product of the likelihood terms for each category. The $\mu\mu$, $\tau_{\text{e}}\tau_\mu$, $\tau_{\text{e}}\tau_{\text{had}}$, $\tau_\mu\tau_{\text{had}}$ and $\tau_{\text{had}}\tau_{\text{had}}$ final states each have a selection with and without a b-tagged jet. The likelihood in each category is a product over bins in the distributions of the MMC or visible mass in the signal and control regions as described in

Sections 5 and 6. Only one bin of visible mass is considered for each Higgs boson mass hypothesis in the $\tau_e\tau_\mu$ final state with a jet veto.

The expected number of events for signal (s_j) and background (b_j), as well as the observed number of events (N_j) in each bin of the mass distributions, enter in the definition of the likelihood function $\mathcal{L}(\mu, \boldsymbol{\theta})$. A "signal strength" parameter (μ) multiplies the expected signal in each bin. The value $\mu = 0$ corresponds to the background-only hypothesis, while $\mu = 1$ corresponds to the signal plus background hypothesis with all Higgs bosons having the masses and cross sections specified by the considered point in the m_A–$\tan\beta$ plane for the MSSM exclusion limit. Signal and background predictions depend on systematic uncertainties that are parametrised by nuisance parameters $\boldsymbol{\theta}$, which in turn are constrained using Gaussian functions, so that

$$\mathcal{L}(\mu, \theta) = \prod_{\substack{\text{j=bin and} \\ \text{category}}} \text{Poisson}\left(N_j \,\middle|\, \mu \cdot s_j + b_j\right) \prod_{\theta} \text{Gaussian}\left(\theta \,|\, 0, 1\right). \tag{8}$$

The correlations of the systematic uncertainties across categories are taken into account. The expected signal and background event counts in each bin are functions of $\boldsymbol{\theta}$. The parametrisation is chosen such that the rates in each channel are log-normally distributed for a normally distributed $\boldsymbol{\theta}$.

The test statistic q_μ is defined as

$$\tilde{q}_\mu = \begin{cases} -2\ln\left(\frac{\mathcal{L}(\mu,\hat{\hat{\boldsymbol{\theta}}}_\mu)}{\mathcal{L}(0,\hat{\hat{\boldsymbol{\theta}}}_0)}\right) & \text{if } \hat{\mu} < 0, \\ -2\ln\left(\frac{\mathcal{L}(\mu,\hat{\hat{\boldsymbol{\theta}}}_\mu)}{\mathcal{L}(\hat{\mu},\hat{\boldsymbol{\theta}})}\right) & \text{if } 0 \le \hat{\mu} \le \mu, \\ 0 & \text{if } \hat{\mu} > \mu, \end{cases} \tag{9}$$

where $\hat{\mu}$ and $\hat{\boldsymbol{\theta}}$ refer to the global maximum of the likelihood and $\hat{\hat{\boldsymbol{\theta}}}_\mu$ corresponds to the conditional maximum likelihood of $\boldsymbol{\theta}$ for a given μ.

To calculate the upper limit, the compatibility of the observed or expected dataset with the signal plus background hypothesis is checked following the modified frequentist method known as CL_s [65]. The asymptotic approximation [66] is used to evaluate the probability density functions rather than performing pseudo-experiments and the procedure has been validated using ensemble tests.

9 Results

No significant excess of events above the background-only expectation is observed in 4.7–4.8 fb^{-1} of $\sqrt{s} = 7$ TeV proton-proton collision data. A 95 % confidence level upper limit on $\tan\beta$ is set for each m_A point using the frequentist method described in Section 8. This is done using Higgs boson cross sections calculated in the m_h^{max} scenario with $\mu > 0$ [9]. Results for each of the $\mu\mu$, $\tau_e\tau_\mu$, $\tau_{\text{lep}}\tau_{\text{had}}$ and $\tau_{\text{had}}\tau_{\text{had}}$ final states, as well as for their statistical combination can be seen in Figure 6.

The outcome of the search is further interpreted in the generic case of a scalar boson ϕ produced in the gluon fusion or b-associated production mode and decaying to $\mu^+\mu^-$ or $\tau^+\tau^-$. Figure 7 shows 95 % CL_s limits based on this interpretation.

10 Summary

A search for the neutral Higgs bosons of the Minimal Supersymmetric Standard Model (MSSM) in proton-proton collisions at a centre-of-mass energy of 7 TeV with the ATLAS experiment at the LHC

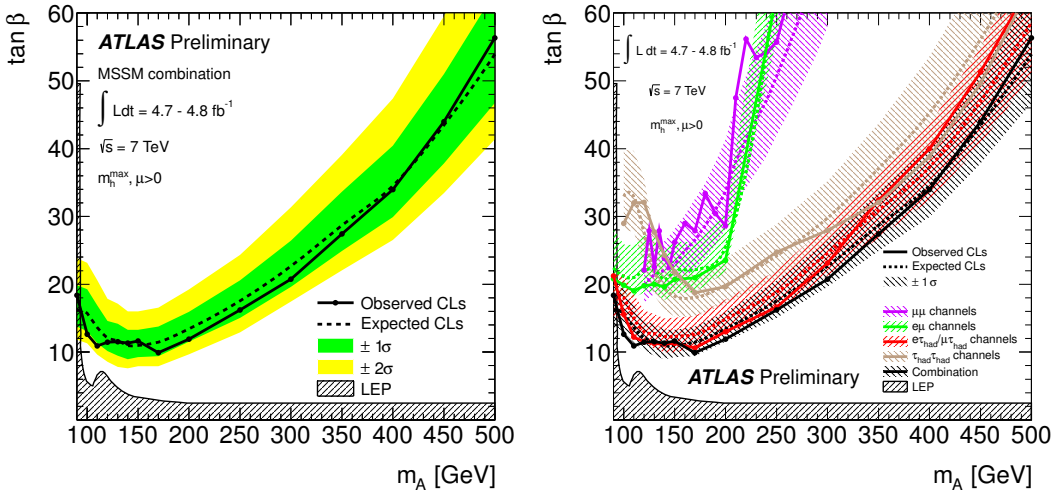

Figure 6: Expected (dashed line) and observed (solid line) 95 % confidence level CL_s limits on $\tan\beta$ as a function of m_A for the statistical combination of all channels along with the $1 \pm \sigma$ (green) and $\pm 2\,\sigma$ (yellow) bands for the expected limit are shown on the left plot. The 95 % confidence level CL_s limits along with the $\pm 1\,\sigma$ band for the expected limit for each of the $\mu\mu$, $\tau_e\tau_\mu$, $\tau_{\text{lep}}\tau_{\text{had}}$ and $\tau_{\text{had}}\tau_{\text{had}}$ final states are shown on the right plot.

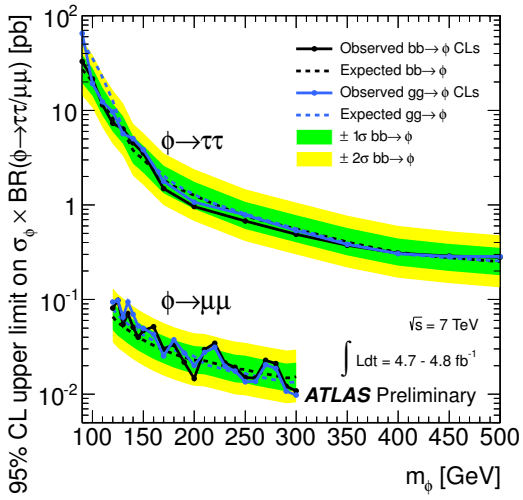

Figure 7: Expected and observed 95 % confidence level CL_s limits on the cross section for gluon-fusion and b-associated Higgs boson production times the branching ratio into τ and μ pairs, respectively along with the $\pm 1\,\sigma$ (green) and $\pm 2\,\sigma$ (yellow) bands for the expected limit. The combinations of all $\tau\tau$ and $\mu\mu$ channels are shown.

is presented. The study is based on a data sample that corresponds to an integrated luminosity of $4.7 - 4.8\,\mathrm{fb}^{-1}$. The decay modes of the Higgs boson considered are $h/A/H \to \mu^+\mu^-$, $h/A/H \to \tau_\mathrm{e}\tau_\mu$, $h/A/H \to \tau_\mathrm{lep}\tau_\mathrm{had}$ and $h/A/H \to \tau_\mathrm{had}\tau_\mathrm{had}$. The analysis selection criteria exploit the two main production mechanisms in the MSSM, the gluon-fusion and b-associated production modes, by introducing categories for event samples with and without an identified b jet. The estimations of the most important backgrounds to this search have been done or confirmed using data-driven control samples. Since no excess of events over the expected background is observed, 95 % confidence level limits are set in the m_A–$\tan\beta$ plane, excluding a significant fraction of the MSSM parameter space.

References

[1] L. Evans and P. Bryant, *JINST* **3** (2008) S08001.

[2] F. Englert and R. Brout, *Phys. Rev. Lett.* **13** (1964) 321.

[3] P. W. Higgs, *Phys. Lett.* **12** (1964) 132.

[4] P. W. Higgs, *Phys. Rev. Lett.* **13** (1964) 508.

[5] P. W. Higgs, *Phys. Rev.* **145** (1966) 1156.

[6] G. S. Guralnik, C. R. Hagen and T. W. B. Kibble, *Phys. Rev. Lett.* **13** (1964) 585.

[7] H. P. Nilles, *Phys. Rep.* **110** (1984) 1.

[8] H. E. Haber and G. L. Kane, *Phys. Rep.* **117** (1985) 75.

[9] M. Carena, S. Heinemeyer, C. E. M. Wagner and G. Weiglein, *Eur. Phys. J.* **C 26** (2003) 601.

[10] ALEPH, DELPHI, L3 and OPAL Collaborations, S. Schael et al., *Eur. Phys. J.* **C 47** (2006) 547.

[11] CDF Collaboration, D0 Collaboration, Tevatron New Physics Higgs Working Group, arXiv:1003.3363.

[12] CDF Collaboration, T. Aaltonen et al., *Phys. Rev. Lett.* **103** (2009) 201801.

[13] D0 Collaboration, V. M. Abazov et al., *Phys. Rev. Lett.* **101** (2008) 071804.

[14] CMS Collaboration, *Phys. Rev. Lett.* **106** (2011) 231801, [arXiv:1104.1619].

[15] ATLAS Collaboration, *Phys. Lett.* **B 705** (2011) 174, [arXiv:1107.5003].

[16] ATLAS Collaboration, arXiv:1207.0319. Submitted to Phys. Rev. D.

[17] CMS Collaboration, arXiv:1202.1488. Submitted to Phys. Lett. B.

[18] S. Heinemeyer, O. Stal, and G. Weiglein *Phys. Lett.* **B710** (2012) 201, [arXiv:1112.3026].

[19] ATLAS Collaboration, *JINST* **3** (2008) S08003.

[20] ATLAS Collaboration, ATLAS-CONF-2011-116. http://cdsweb.cern.ch/record/1376384.

[21] ATLAS Collaboration, *Eur. Phys. J.* **C 71** (2011) 1630, [arXiv:1101.2185].

[22] M. Spira, hep-ph/9510347.

[23] R. V. Harlander and W. B. Kilgore, *Phys. Rev. Lett.* **88** (2002) 201801.

[24] R. Harlander, M. Krämer and M. Schumacher, arXiv:1112.3478.

[25] S. Dittmaier, M. Krämer and M. Spira, *Phys. Rev.* **D 70** (2004) 074010.

[26] S. Dawson, C. B. Jackson, L. Reina and D. Wackeroth, *Mod. Phys. Lett.* **A 21** (2006) 89.

[27] R. Harlander and W. B. Kilgore, *Phys. Rev.* **D 68** (2003) 013001.

[28] M. Frank, T. Hahn, S. Heinemeyer, W. Hollik, and H. Rzehak et al., *JHEP* **0702** (2007) 047, [hep-ph/0611326].

[29] LHC Higgs Cross Section Working Group, S. Dittmaier, C. Mariotti, G. Passarino, R. Tanaka (Eds.) et al., arXiv:1101.0593.

[30] S. Alioli et al., *JHEP* **02** (2009) 029.

[31] T. Gleisberg et al., *JHEP* **02** (2009) 007.

[32] ATLAS Collaboration, *Eur. Phys. J.* **C 70** (2010) 823, [arXiv:1005.4568].

[33] GEANT4 collaboration, S. Agostinelli et al., *Nucl. Instrum. Meth.* **A 506** (2003) 250.

[34] M. L. Mangano et al., *JHEP* **07** (2003) 001.

[35] T. Sjostrand, S. Mrenna and P. Skands, *JHEP* **05** (2006) 026.

[36] C. Anastopoulos et al., *Journal of Physics: Conference Series* **119** (2008) 032003.

[37] S. Frixione and B. R. Webber, *JHEP* **06** (2002) 029.

[38] B. P. Kersevan and E. Richter-Was, hep-ph/0405247.

[39] G. Corcella et al., *JHEP* **01** (2001) 010.

[40] J. M. Butterworth, J. R. Forshaw and M. H. Seymour, *Z. Phys.* **C 72** (1996) 637.

[41] T. Binoth, M. Ciccolini, N. Kauer and M. Krämer, *JHEP* **12** (2006) 046.

[42] H.-L. Lai et al., *Phys. Rev.* **D 82** (2010) 074024.

[43] J. Pumplin, *JHEP* **0207** (2002) 012.

[44] A. Sherstnev and R. S. Thorne, *Eur. Phys. J.* **C 55** (2008) 553.

[45] S. Jadach, J. H. Kuhn and Z. Was, *Comput. Phys. Commun.* **64** (1990) 275.

[46] E. Barberio, B. V. Eijk and Z. Was, *Comput. Phys. Commun.* **66** (1991) 115.

[47] ATLAS Collaboration, *Eur. Phys. J.* **C 72** (2012) 1909, [arXiv:1110.3174].

[48] ATLAS Collaboration, ATLAS-CONF-2011-063. http://cdsweb.cern.ch/record/1345743.

[49] M. Cacciari, G. P. Salam and G. Soyez, *JHEP* **04** (2008) 063, [arXiv:0802.1189].

[50] W. Lampl et al., ATL-LARG-PUB-2008-002.

[51] ATLAS Collaboration, arXiv:1112.6426.

[52] ATLAS Collaboration, ATLAS-CONF-2011-159. http://cdsweb.cern.ch/record/1403179.

[53] D0 collaboration, V. M. Abazov et al., *Phys.Rev.* **D76** (2007) 072007, [hep-ex/0612040].

[54] ATLAS Collaboration, ATLAS-CONF-2012-043. http://cdsweb.cern.ch/record/1435197.

[55] ATLAS Collaboration, ATLAS-CONF-2011-152. http://cdsweb.cern.ch/record/1398195.

[56] ATLAS Collaboration, *Eur. Phys. J.* **C 72** (2012) 1844, [arXiv:1108.5602].

[57] K. Nakamura et al. (Particle Data Group), *J. Phys.* **G 37** (2010) 075021.

[58] ATLAS Collaboration, ATLAS-CONF-2011-132. http://cdsweb.cern.ch/record/1383835.

[59] ATLAS Collaboration, ATLAS-CONF-2011-113. http://cdsweb.cern.ch/record/1375550.

[60] A. Elagin, P. Murat, A. Pranko and A. Safonov, *Nucl.Instrum.Meth.* **A654** (2011) 481, [arXiv:1012.4686].

[61] ATLAS Collaboration, ATLAS-CONF-2011-046. http://cdsweb.cern.ch/record/1338575.

[62] ATLAS Collaboration, ATLAS-CONF-2012-043. http://cdsweb.cern.ch/record/1435194.

[63] ATLAS Collaboration, ATLAS-CONF-2012-040. http://cdsweb.cern.ch/record/1435194.

[64] ATLAS Collaboration, ATLAS-CONF-2012-006. http://cdsweb.cern.ch/record/1426991.

[65] A. L. Read, *J. Phys.* **G 28** (2002) 2693.

[66] G. Cowan, K. Cranmer, E. Gross and O. Vitells, *Eur. Phys. J.* **C 71** (2011) 1554, [arXiv:1007.1727].

A Appendix

A.1 Individual exclusion limits

The individual 95 % confidence level cross section exclusion limits of all Higgs boson decay channels and final states are shown in Figure 8. Similarly, Figure 9 shows the 95 % exclusion limits in the m_{A}–$\tan\beta$ plane.

A.2 Additional plots for $h/A/H \to \mu^+\mu^-$

Figure 10 shows the signal model for $m_{\mathrm{A}} = 150$ GeV and $\tan\beta = 40$ separately for the gluon-fusion and the b quark associated production modes. The resonances for the single h, A and H contributions are obtained with the interpolation procedure. The masses, widths and cross sections are set to their theoretical predictions for the m_h^{max} scenario with $\mu > 0$. The invariant mass distribution for $A \to \mu^+\mu^-$, simulated for this m_{A}–$\tan\beta$ point, is also shown for comparison.

A.3 Additional plots for $h/A/H \to \tau_{\mathrm{e}}\tau_{\mu}$

Figure 11 shows the jet multiplicity distribution and Figure 12 the p_{T} distributions for electrons and muons for the jet-vetoed selection after the requirement of exactly zero jets in the central detector region ($|\eta| < 2.5$). Table 7 shows the observed and expected event yields in the different mass windows considered for the jet-veto channel.

The variable $\sum_{\ell=e,\mu} \cos\Delta\phi_{E_{\mathrm{T}}^{\mathrm{miss}},\ell}$ is shown in Figure 13 (left) after preselection, b jet selection and cut on the sum of the lepton transverse momenta and the missing transverse energy and H_T is shown (right) with the addition of a cut on $\sum_{\ell=e,\mu} \cos\Delta\phi_{E_{\mathrm{T}}^{\mathrm{miss}},\ell}$.

Figure 14 shows the distribution m_{MMC} in the $t\bar{t}$ control region of the b-tagged selection (see Section 6.2). Note that the $t\bar{t}$ normalisation is obtained from data in this figure.

A.4 Additional plots for $h/A/H \to \tau_{\mathrm{lep}}\tau_{\mathrm{had}}$

Figure 15 (a) shows the transverse mass distribution for the combined electron and muon samples after selecting the lepton and τ_{had} and the opposite charge sign requirement. The transverse momentum of the selected b jet in the b-tagged selection is shown in Figure 15 (b).

A.5 Additional plots for $h/A/H \to \tau_{\mathrm{had}}\tau_{\mathrm{had}}$

Figure 16 (a) shows the missing transverse momentum distribution after the b-tagged selection. The angular distance in the transverse plane between the two selected hadronic τ decays is shown in Figure 16 (b). In Figure 17 the transverse momentum distributions for the leading and next-to-leading hadronic τ decay are shown.

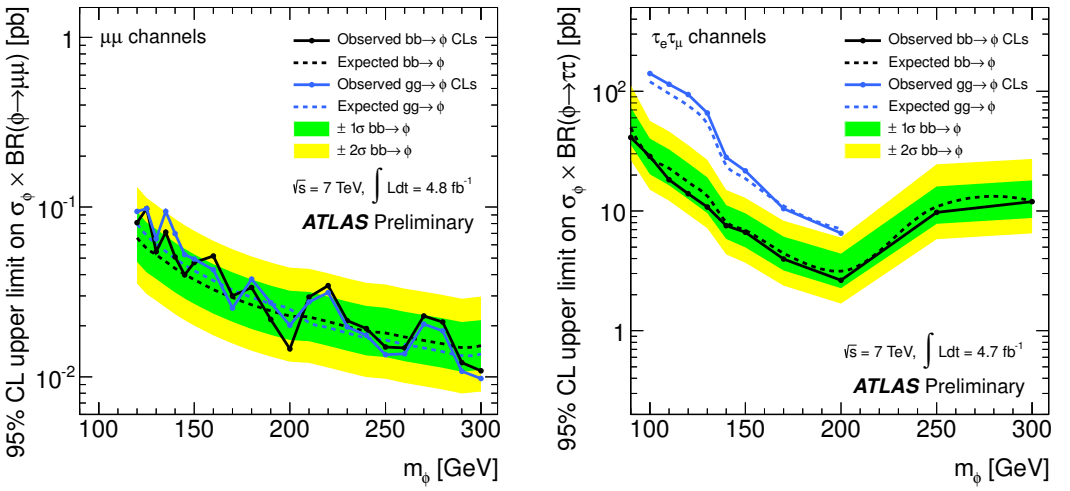

(a) $h/A/H \to \mu^+\mu^-$ (b) $h/A/H \to \tau_e\tau_\mu$

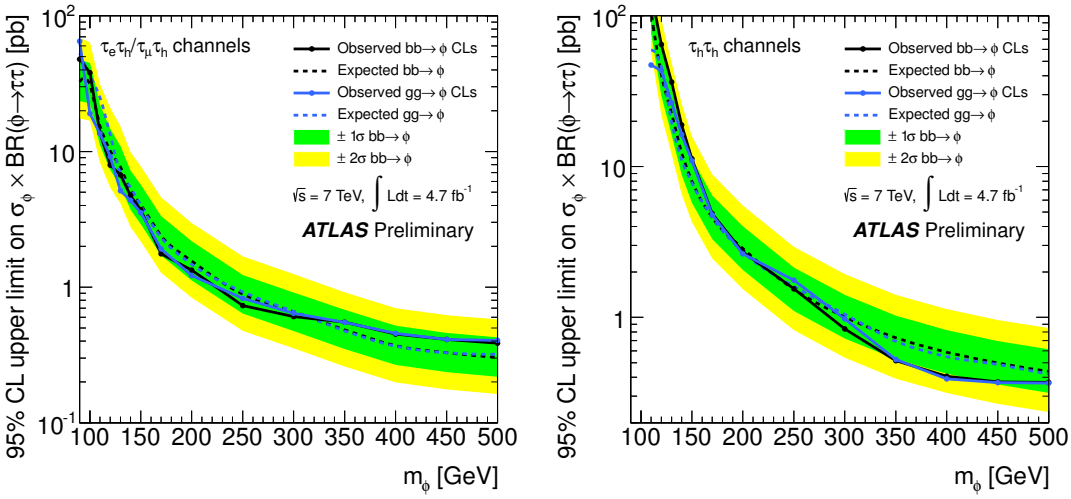

(c) $h/A/H \to \tau_{\text{lep}}\tau_{\text{had}}$ (d) $h/A/H \to \tau_{\text{had}}\tau_{\text{had}}$

Figure 8: Expected (dashed line) and observed (solid line) 95 % confidence level cross section exclusion limits as a function of m_ϕ, along with the $\pm 1\,\sigma$ (green) and $\pm 2\,\sigma$ bands of the expected limit. Subfigure (a) shows the limits for the decay into μ pairs. The limits for the decay into τ pairs are shown in Subfigures (b), (c) and (d) for the $\tau_e\tau_\mu$, the combined $\tau_e\tau_{\text{had}}$ and $\tau_\mu\tau_{\text{had}}$ and the $\tau_{\text{had}}\tau_{\text{had}}$ final states, respectively.

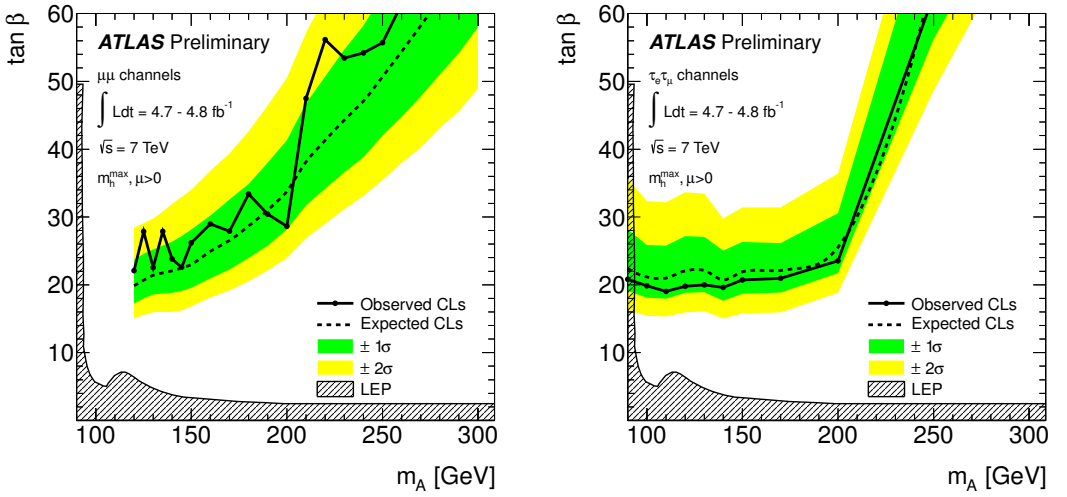

(a) $h/A/H \to \mu^+\mu^-$

(b) $h/A/H \to \tau_e\tau_\mu$

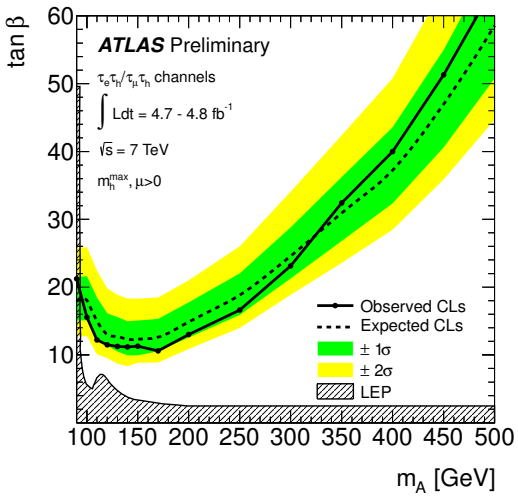

(c) $h/A/H \to \tau_{\mathrm{lep}}\tau_{\mathrm{had}}$

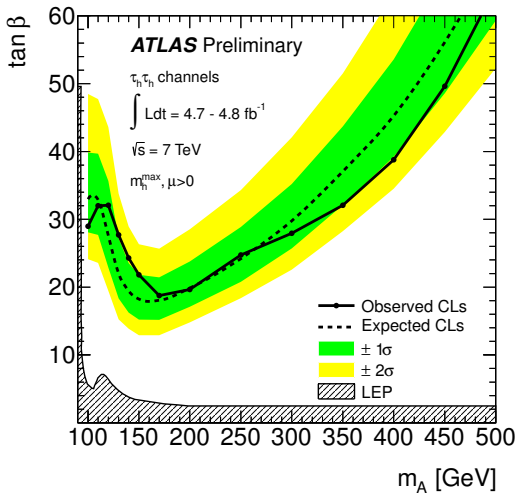

(d) $h/A/H \to \tau_{\mathrm{had}}\tau_{\mathrm{had}}$

Figure 9: Expected (dashed line) and observed (solid line) 95 % confidence level exclusion limits of $\tan\beta$ as a function of m_{A}, along with the $\pm 1\,\sigma$ (green) and $\pm 2\,\sigma$ bands of the expected limit. Subfigure (a) shows the limits for the $h/A/H \to \mu^+\mu^-$ channel. The limits for the $h/A/H \to \tau^+\tau^-$ decay channel are shown in Subfigures (b), (c) and (d) for the $\tau_{\mathrm{e}}\tau_\mu$, the combined $\tau_{\mathrm{e}}\tau_{\mathrm{had}}$ and $\tau_\mu\tau_{\mathrm{had}}$ and the $\tau_{\mathrm{had}}\tau_{\mathrm{had}}$ final states, respectively.

	m_A = 100 GeV	m_A = 110 GeV	m_A = 120 GeV	m_A = 130 GeV
mass window	[30, 88] GeV	[36, 98] GeV	[46, 106] GeV	[54, 112] GeV
$Z/\gamma^* \to \tau^+\tau^-$	8030±50 ±680	7550±40 ±640	5440±40 $^{+470}_{-460}$	3340±30 $^{+320}_{-290}$
W + jets	61±16 $^{+5}_{-17}$	69±16 $^{+6}_{-17}$	80±17 $^{+7}_{-17}$	55±12 $^{+6}_{-7}$
$Z/\gamma^* \to \ell^+\ell^-$	61.3±6.1$^{+6.1}_{-4.8}$	68.2±6.5 $^{+6.5}_{-5.3}$	63.7±6.1 $^{+6.2}_{-5.0}$	58.9±5.9$^{+5.9}_{-4.6}$
$t\bar{t}$	14.3±0.7$^{+2.3}_{-2.3}$	19.0±0.8 $^{+3.2}_{-3.2}$	22.8±0.8 $^{+3.9}_{-4.0}$	25.2±0.9$^{+4.1}_{-4.5}$
Single top	8.1±0.9$^{+1.0}_{-1.2}$	10.3±1.0 $^{+1.3}_{-1.5}$	12.5±1.1 $^{+1.6}_{-1.8}$	12.2±1.1$^{+1.6}_{-1.6}$
Di-boson	279±3 $^{+26}_{-27}$	345±3 $^{+32}_{-33}$	375±4 ±35	380±4 $^{+35}_{-36}$
Multi-jet	459±21 $^{+35}_{-52}$	350±20 $^{+27}_{-39}$	200±18 $^{+16}_{-19}$	144±14 ±13
Total	8910±50 $^{+680}_{-690}$	8420±50 ±640	6190±50 $^{+470}_{-460}$	4010±40 $^{+320}_{-290}$
$b\bar{b}h/A/H \to \tau\tau$	421±17 $^{+60}_{-79}$	365±8 $^{+49}_{-65}$	286±13 $^{+37}_{-48}$	210±10 $^{+26}_{-34}$
$gg \to h/A/H \to \tau\tau$	295±42 $^{+48}_{-46}$	227±32 $^{+37}_{-35}$	147±21 ±23	97±14 ±14
Data	9241	8770	6508	4232

	m_A = 140 GeV	m_A = 150 GeV	m_A = 170 GeV	m_A = 200 GeV
mass window	[70, 114] GeV	[70, 120] GeV	[76, 122] GeV	[80, 140] GeV
$Z/\gamma^* \to \tau^+\tau^-$	680±14 $^{+85}_{-73}$	685±14 $^{+85}_{-74}$	302±9 $^{+47}_{-41}$	176±7 $^{+25}_{-21}$
W + jets	44±11 $^{+5}_{-6}$	47±11 $^{+5}_{-6}$	36.0±9.6 $^{+4.6}_{-2.9}$	32.6±9.2$^{+4.0}_{-2.4}$
$Z/\gamma^* \to \ell^+\ell^-$	45.9±5.1$^{+4.1}_{-3.6}$	45.9±5.1 $^{+4.1}_{-3.6}$	36.0±4.5 $^{+3.0}_{-2.8}$	29.2±4.1$^{+2.4}_{-2.2}$
$t\bar{t}$	20.8±0.8$^{+3.5}_{-3.8}$	23.4±0.9 $^{+3.9}_{-4.2}$	22.2±0.8 $^{+3.5}_{-4.0}$	28.4±0.9$^{+4.6}_{-5.1}$
Single top	10.7±1.0$^{+1.4}_{-1.3}$	11.9±1.0 $^{+1.5}_{-1.5}$	11.2±1.0 $^{+1.4}_{-1.5}$	14.2±1.1$^{+2.0}_{-2.2}$
Di-boson	293±3 $^{+27}_{-28}$	325±3 $^{+30}_{-31}$	294±3 $^{+27}_{-28}$	346±3 $^{+32}_{-33}$
Multi-jet	52±11 $^{+8}_{-5}$	59.7±11.6$^{+8.7}_{-5.8}$	51.3±10.6$^{+5.5}_{-6.1}$	55±11 $^{+6}_{-7}$
Total	1146±22 $^{+90}_{-78}$	1197±22 $^{+91}_{-80}$	753±18 $^{+55}_{-50}$	681±17 $^{+42}_{-40}$
$b\bar{b}h/A/H \to \tau\tau$	107±6 $^{+13}_{-17}$	105±6 $^{+12}_{-16}$	73±4 $^{+8}_{-11}$	53.2±3.1$^{+5.9}_{-7.3}$
$gg \to h/A/H \to \tau\tau$	44.8±6.5$^{+6.7}_{-6.6}$	41.6±5.9 $^{+6.4}_{-6.3}$	23.9±3.4 $^{+3.9}_{-3.9}$	13.8±2.0$^{+2.6}_{-2.7}$
Data	1195	1245	751	666

Table 7: Expected background and hypothetical signal event yields and observed event yields in data in the different visible mass windows with the statistical and systematic uncertainties. The signal expectation is shown for the MSSM parameter point with $\tan\beta = 20$.

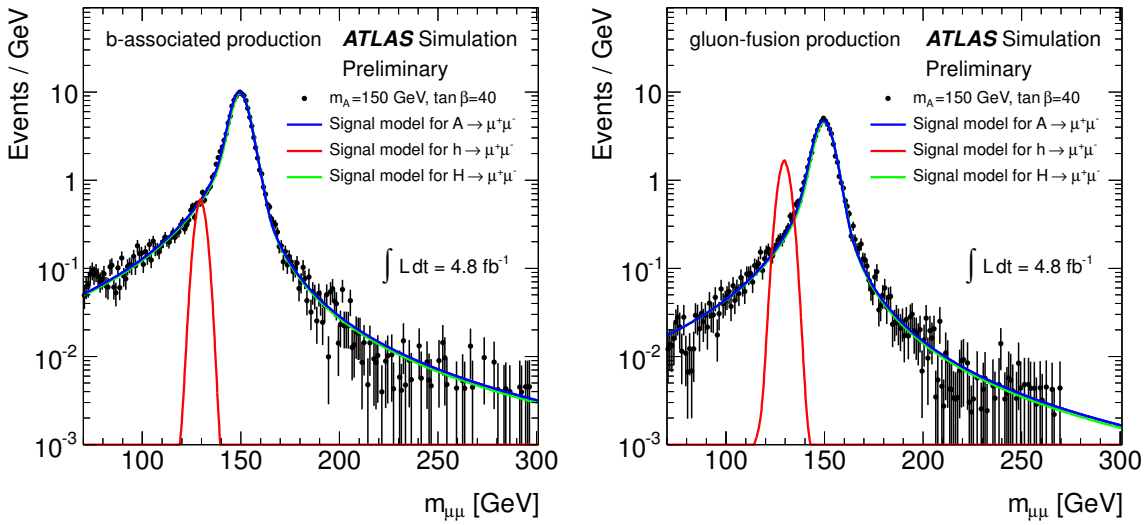

Figure 10: Signal model containing contributions from h (red), A (blue) and H (green) obtained from the interpolation procedure shown for the signal mass point at $m_A = 150$ GeV and $\tan\beta = 40$ produced in association with b quarks (left-hand side) and in gluon-fusion (right-hand side). The masses, widths and cross sections are set to their theoretical predictions in the m_h^{max} scenario with $\mu > 0$. The invariant mass distribution (solid circles) for the simulated process $A \to \mu^+\mu^-$ is shown for comparison.

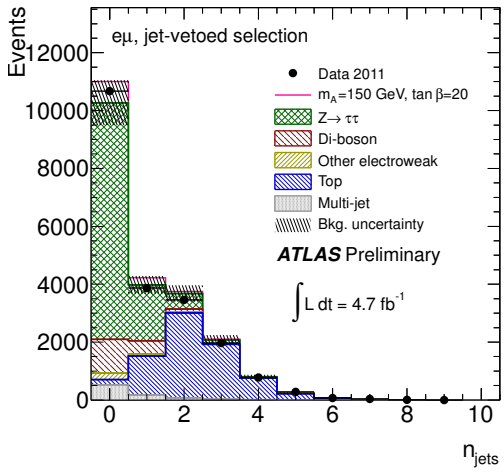

Figure 11: Distribution of the jet multiplicity after the requirement of exactly zero jets in the event for the jet-vetoed selection in the $h/A/H \to \tau_e\tau_\mu$ channel. The data are compared to the background expectation and an added hypothetical MSSM signal ($m_A = 150$ GeV, $\tan\beta = 20$). The background uncertainties include statistical and systematic uncertainties.

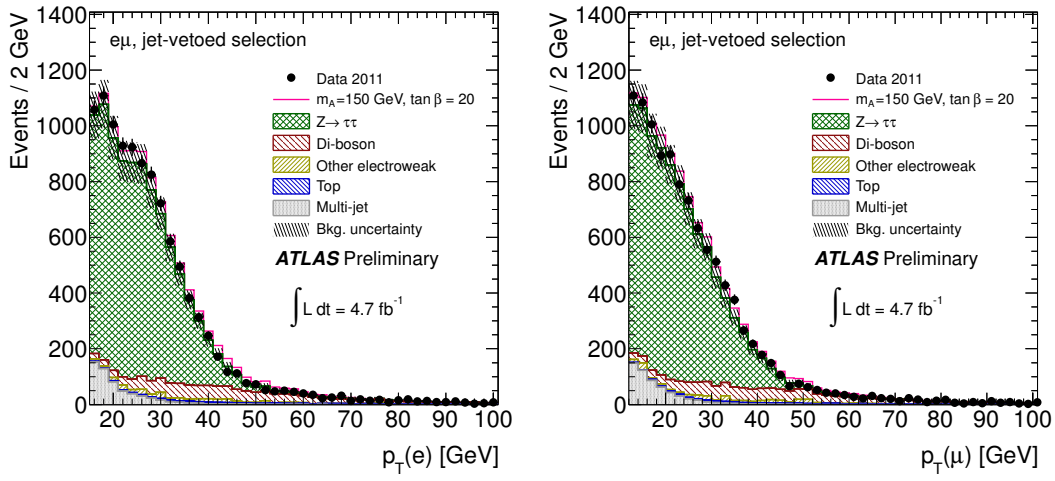

(a) electron p_{T} (b) muon p_{T}

Figure 12: Distribution of thetransverse momentum of the electron (a) and muon (a) after the requirement of exactly zero jets in the event for the jet-vetoed selection in the $h/A/H \rightarrow \tau_{\mathrm{e}}\tau_{\mu}$ channel. The data are compared to the background expectation and an added hypothetical MSSM signal ($m_{\mathrm{A}} = 150$ GeV, $\tan\beta = 20$). The background uncertainties include statistical and systematic uncertainties.

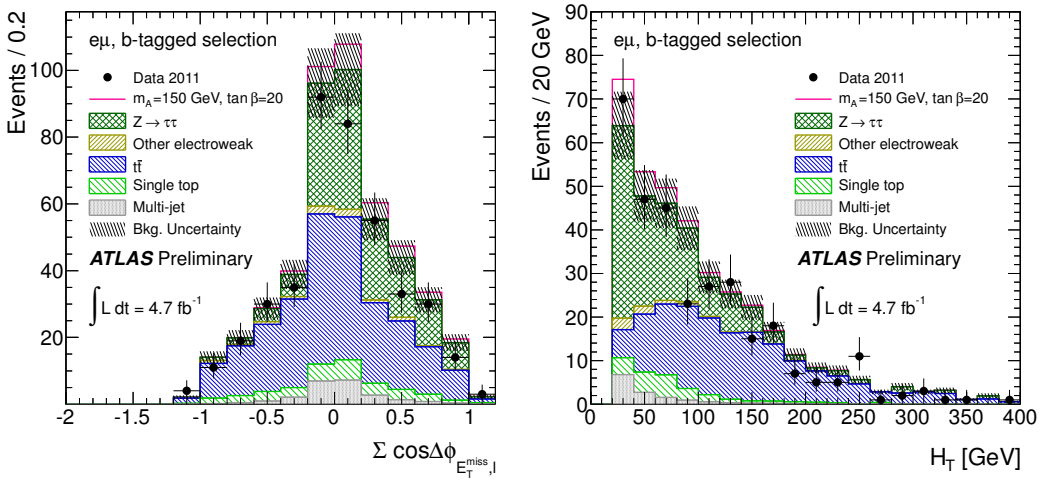

Figure 13: Distribution of the $\sum \cos\Delta\phi_{E_{\mathrm{T}}^{\mathrm{miss}},l}$ variable (left) and the sum of the transverse energies of all jets with $p_T > 20$ GeV, H_T (right) in the b-tagged selection of the $h/A/H \rightarrow \tau_{\mathrm{e}}\tau_{\mu}$ channel. $\sum_{\ell=e,\mu}\cos\Delta\phi_{E_{\mathrm{T}}^{\mathrm{miss}},\ell}$ is shown after the preselection, the b jet selection and the cut on the sum of the lepton transverse momenta and missing transverse energy. H_T is shown after the preselection, the b jet selection, the cut on the sum of the lepton transverse momenta and missing transverse energy and the cut on $\sum_{\ell=e,\mu}\cos\Delta\phi_{E_{\mathrm{T}}^{\mathrm{miss}},\ell}$. The data are compared to the background expectation and an added hypothetical MSSM signal ($m_{\mathrm{A}} = 150$ GeV, $\tan\beta = 20$). The background uncertainty includes the statistical and systematic uncertainties.

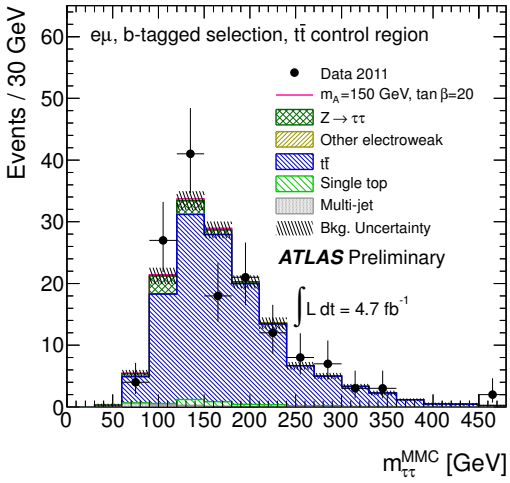

Figure 14: Distribution of the MMC mass in the $t\bar{t}$ control region of the b-tagged selection sample after the full event selection in the $h/A/H \to \tau_e\tau_\mu$ channel. The data are compared to the background expectation and an added hypothetical MSSM signal ($m_A = 150$ GeV, $\tan\beta = 20$). The background uncertainty includes the statistical uncertainty only.

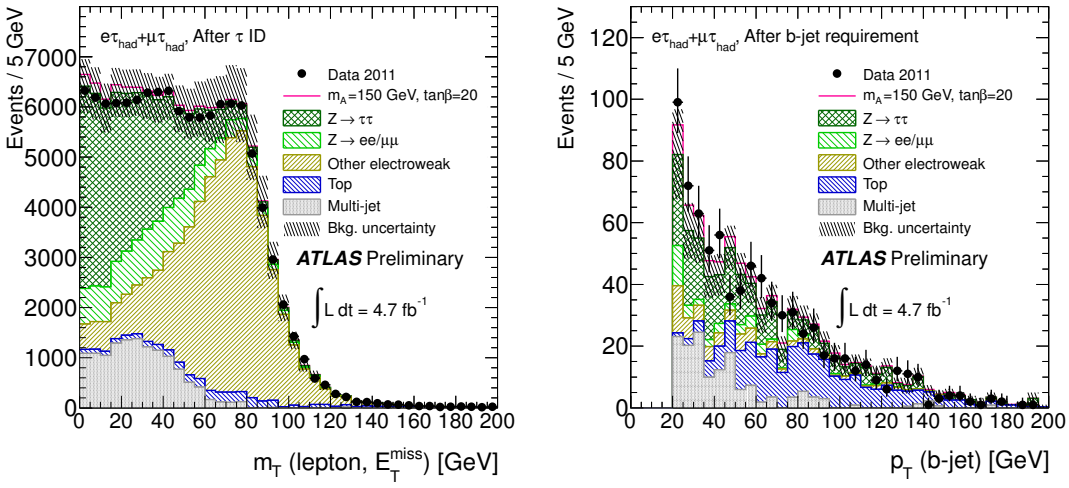

(a) m_{T} (b) b jet p_{T}

Figure 15: Transverse mass m_{T} (a) after the τ selection and the requirement of opposite sign of the charges of lepton and hadronic τ decay and the transverse momentum of the selected b jet in the b-tagged selection (b) for the $h/A/H \to \tau_{\mathrm{lep}}\tau_{\mathrm{had}}$ channel. The data are compared to the background expectation and an added hypothetical MSSM signal ($m_A = 150$ GeV, $\tan\beta = 20$). The background uncertainties include the statistical and the systematic uncertainties.

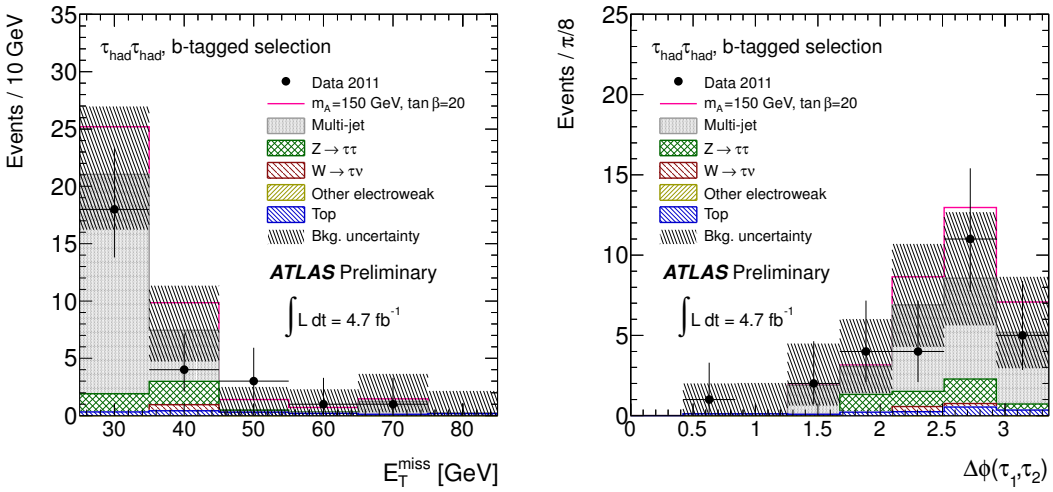

(a) $E_{\mathrm{T}}^{\mathrm{miss}}$ (b) $\Delta\phi(\tau_1, \tau_2)$

Figure 16: Missing transverse momentum (a) and angular distance in the transverse plane between the two selected hadronic τ decays (b) for the b-tagged selection of the $h/A/H \rightarrow \tau_{\mathrm{had}}\tau_{\mathrm{had}}$ channel. The data are compared to the background expectation and an added hypothetical MSSM signal ($m_{\mathrm{A}} = 150$ GeV, $\tan\beta = 20$). The background uncertainty includes the statistical and the systematic uncertainties.

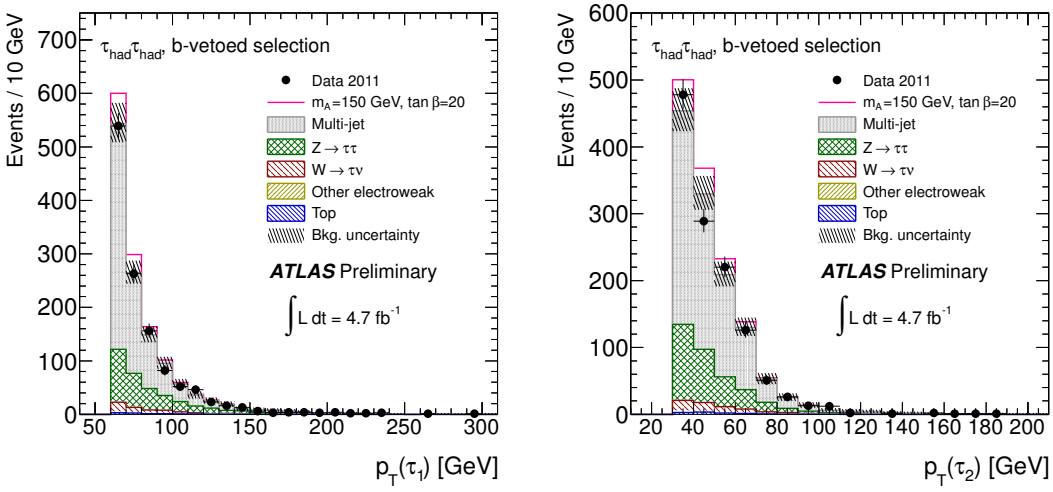

(a) Leading τ_{had} p_{T} (b) Next-to-leading τ_{had} p_{T}

Figure 17: Transverse momentum of the leading (a) and next-to-leading (b) hadronic τ decay for the b-vetoed selection of the $h/A/H \rightarrow \tau_{\mathrm{had}}\tau_{\mathrm{had}}$ channel. The data are compared to the background expectation and an added hypothetical MSSM signal ($m_{\mathrm{A}} = 150$ GeV, $\tan\beta = 20$). The background uncertainty include the statistical and the systematic uncertainties.